Short-Term Innovative and Exploratory Research Projects

ALPHA FOUNDATION FOR THE IMPROVEMENT OF
MINE SAFETY AND HEALTH

Final Technical Report

1.0 COVER PAGE

Project Title: Development of a Gas and Dust Explosion Model

Organization Name: West Virginia University (WVU)

Principle Investigator: Prof. V'yacheslav (Slava) Akkerman

Contact Information: Email: Vyacheslav.Akkerman@mail.wvu.edu

Phone: 304-293-0802;   Fax: 304-293-6682

Other WVU Personnel: Sinan Demir (Graduate Student)

Sri Hari Ramakrishna Chalagalla (Graduate Student)

Jad Sadek (Graduate Student)

Organization Name: Worcester Polytechnic Institute (WPI)

Co-PI: Prof. Ali S. Rangwala

Contact Information: Email: Rangwala@wpi.edu

Phone: 508-831-6409;   Fax: 508-622-6983

Other WPI Personnel: Sreenivasan Ranganathan (Graduate Student)

Full Period of Performance: May 1, 2014 – July 31, 2015

ACKNOWLEDGEMENT/DISCLAIMER

2.0 EXECUTIVE SUMMARY

This one and half year project developed the building blocks for a fully compressible Computational Fluid Dynamics (CFD) solver capable of solving gas and dust deflagrations as found during coal mining accidents. Reliable input parameters that can characterize the dust –gas – air mixture were necessary for the modeling effort. Towards this end, a new experimental platform capable of measuring laminar and turbulent burning velocities of coal dust-methane-air flames was designed, constructed and tested during the study. Additives such as inert sand particles were also tested to fundamentally investigate the effect of inert particles on the flame propagation. Finally, a simplified engineering solver that can be used to design explosion vents for industrial applications was also developed.

Details of the (a) CFD model for gas explosions, (b) CFD model for dust explosions, (c) experimental platform for dust flame characterization, and (d) engineering solver for explosion venting can be found in the 3 peer reviewed publications and 10 conference papers that resulted as part of this work. An executable version of the engineering solver can be downloaded from http://combustionlab.wpi.edu/EVA.html

The study was a joint collaborative project between University of West Virginia (Prof. V'yacheslav Akkerman) and Worcester Polytechnic Institute (Prof. Ali S. Rangwala).

3.0 PROBLEM STATEMENT AND INNOVATION OBJECTIVE

Accidental gas and dust explosions represent a hazard to both personnel and equipment in industries dealing with explosive materials. Among them, coal mining industry has, historically, one of the highest fatality and injury rates. Recent mining catastrophes, worldwide, demonstrate that the present test standards (see Appendix A) do not provide an acceptable level of risk.

In particular, modern coal-mining machinery has significantly increased the portion of small-size coal dust collected in intake/return airways, thereby providing a substantial impact on the coal dust propagation speed in the combustible methane-air flow, and the resulting explosion. Most of existing CFD explosion models are fairly expensive, with inability of viewing and modifying the source code. Moreover, notable codes often utilize empirical correlations between various combustion and hydrodynamic parameters e.g. the laminar and turbulent burning rates, the turbulent intensity and the integral length scale. Then these models are linked to particular configurations and therefore require the experimental quantification of the phenomenological coefficients in each particular case. Besides, switching from a homogeneous to a dust-air environment may substantially modify (or break) the very empirical dependence, and thereby requires a qualitatively new consideration, preferably, to be addressed from a fundamental viewpoint.

The logical next step in this direction – redesign the industrial standard test apparatus (see Appendix A) to account for current advances in fundamental science related to the topic and implement the experimental findings towards development of a numerical model – constituted the focus of the present project. The developing computational platform is aimed to be further used to assess the outcome of new designs and technologies employed in the coal mining industry on the probability of ignition, deflagration (flame) propagation and likelihood of the deflagration-to-detonation transition (DDT) in coal mining.

In a narrower viewpoint, the primary goal of the project was to develop a computational platform for gas and dust explosions in applications of serious hazards to life and property such as coal mines. The platform is based on a robust Navier-Stokes code solving fully-compressible

hydrodynamics and combustion equations. The platform has been enriched by incorporating inert and combustible dust, their various distributions, and turbulence models in the Nvaier-Stokes consideration. The development of the computational platform was coordinated with analytical investigations and experimental measurements. Overall, the work was divided into two Phases:

<u>Phase I</u>: Development of a numerical modeling platform to create a Gas Explosion Model (GEM) and a Dust and Gas Explosion Model (D-GEM).

<u>Phase II</u>: Design and construction of an experimental platform to validate and provide input parameters such as laminar and turbulent burning rates for the numerical model.

As a scientific problem, the project involved new fundamental questions about the interaction of particles with a turbulent flow field as well as chemical reaction in multiphase flows. Plus new ideas have also been employed towards modeling of turbulent gas explosions. The uniqueness of the study is in the fact that the physical understanding of the controlling mechanisms associated with particle-air flames had not been explored in depth. To complement the numerical modeling, the analytical predictive scenario of the mining fire evolution, involving several intermediate stages of a fire, as well as the effect of combustible and intern particles, its size and concentration, has been developed. Besides, extensive experimental data of laminar and turbulent burning velocity have been generated during this study. These included gaseous flames as well as particle-air flames, with as a function of particle type, size, concentration, turbulent intensity and length scale identified and tabulated. Apart from this project itself, these experimental data are aimed to be employed further to develop new and extend existing models for turbulent premixed flames mixed with particles.

4.0 RESEARCH APPROACH

4.1. Predictive Scenario for a Methane-air-dust Fire in a Coal Mine

Various sources of flame corrugation and acceleration in tunnels/channels are presented in the table on the right. We have thereby developed a predictive quantitative scenario for a methane-air-dust fire in a coal mine accident. The major stages of the fire evolution are the following.

Origin of flame corrugation/acceleration	Re-dependence	Relevance to mines
Flame Instability	YES, ↑ Re	YES
Finger Flame	NO	YES
Wall Friction	YES, ↓ Re	NO
Obstacles	NO	It depends
Turbulence	YES	YES

1) Initial quasi-spherical expansion of a centrally-ignited flame embryo, with a transformation of an original smoothly-spherical kernel into a globally-spherical, cellular (corrugated) flame structure, due to the hydrodynamic (Darrieus-Landau; DL) combustion instability. Such a flame accelerates in a self-similar manner. In typical mining geometry, the flame velocity can rise by an order of magnitude during this stage. This process is illustrated in Fig. 4.1.1.
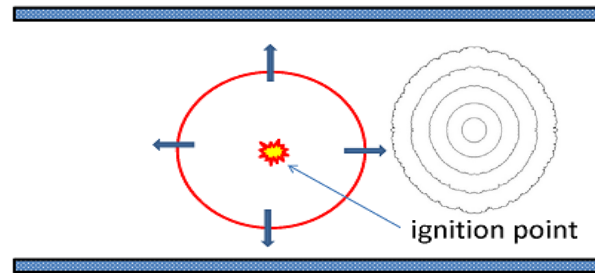

Figure 4.1.1 (stage 1): a globally-spherical expanding flame: ignition, uniform propagation of a smooth front and self-similar acceleration of a cellular front.

2) The so-called "finger-flame" propagation as illustrated in Fig. 4.1.2. This mechanism is scale-invariant, and thereby it is relatively easy to model. The flame velocity raises by one more order of magnitude at this stage. In typical mines, this mechanism is related to the strongest acceleration rate. However, this stage terminates as soon as a flame "skirt" contacts a tunnel wall.
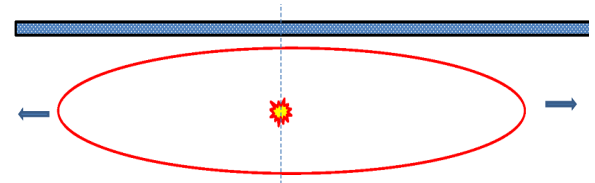

Figure 4.1.2 (stage 2): finger-like flame acceleration.

3) Large-scale-based acceleration due to wall friction and/or obstacles as illustrated in Fig. 4.1.3. The wall friction mechanism weakens with tunnel diameter. Thus, being significant in micro-pipes, this effect is minor in mining passages. In contrast, the obstacle-based acceleration is scale-invariant, and thereby it would provide ultra-fast acceleration for the obstacle size compared to that of the mining passage diameter. However, obstacles are typically small in mines, say, up to 10-20 cm, such that the blockage ratio (the obstacle to tunnel scales ratio) does not exceed 10%, while it should be, say, 30-80% to be important. Thus, the flame accelerations at the 3rd and 4th stages are moderate.
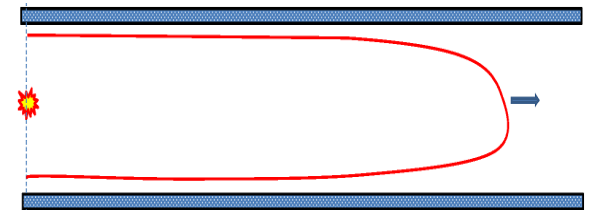

Figure 4.1.3 (stages 3, 4): Effect of wall friction and obstacles.

At all these stages, we have quantified the key characteristics of fire evolution such as the flame shape and propagation velocity; the flame-generated flow velocity field; the timing associated with each stage; and eventually the possibility of the deflagration-to-detonation transition (DDT), with the determination of the DDT time/locus if it occurs.

The major thermal-chemical input parameters for the formulation are the unstretched laminar flame speed; the thermal expansion factor (coupled to the equivalence ratio of the methane-air mixture); the transport coefficients (heat conductivity, diffusivity and viscosity); and the dust characteristics such as the size, heat capacity and concertation of the dust particles. The hydrodynamic input parameters are coupled to the size and configuration of a mining passage.

4.2. Development of the Computational Platform

The analytical formulation has been developed in coordination with that of the computational platform capable of quantifying the probability and associated hazards of spontaneous ignition, dynamics and morphology of a deflagration (flame) front, as well as the likelihood of a DDT in gaseous and dust-gas environments (**GEM** and **D-GEM**) respectively. The backbone of the platform is a robust "in-house" Navier-Stokes code of our group that solves fully-compressible hydrodynamics and combustion equations. The numerical scheme is second-order accurate in time, fourth-order in space for the convective terms, and second order in space for the diffusive term. The platform has a self-adaptive structured computational grid, which makes it suitable to simulate the domains with large aspect ratio such as mine tunnels. The solver is available in a two-dimensional (Cartesian and cylindrical axisymmetric) version as well as a three-dimensional Cartesian version. The platform is adapted for parallel (MPICH) commutations. It is noted that the very embryo of the platform was developed originally at Volvo Aero, and it has subsequently been updated, comprehensively, by several research groups in Sweden and the U.S. This embryonic core of the platform has been justified by successful employment in modeling of various practical aero-acoustic and combustion applications. The basic equations read

$$\frac{\partial \rho}{\partial t} + \frac{\partial}{\partial x_i}\left(\rho u_i\right) = 0; \quad \frac{\partial}{\partial t}\left(\rho u_i\right) + \frac{\partial}{\partial x_j}\left(\rho u_i u_j + \delta_{ij} p - \gamma_{ij}\right) = 0,$$

$$\frac{\partial}{\partial t}\left(\rho \varepsilon + \frac{1}{2}\rho u_i u_i\right) + \frac{\partial}{\partial x_j}\left(\rho u_j h + \frac{1}{2}\rho u_i u_i u_j + q_j - u_i \gamma_{ij}\right) = 0, \quad (4.2.1)$$

$$\frac{\partial}{\partial t}\left(\rho Y\right) + \frac{\partial}{\partial x_i}\left(\rho u_i Y - \frac{\zeta}{Sc}\frac{\partial Y}{\partial x_i}\right) = -\frac{\rho Y}{\tau_R}\exp(-E / R_p T),$$

Combustion is characterized by the planar flame speed S_L and its thickness L_f. While the system (1) generally describes a homogenous fluid, we implemented the noncombustible dust particles by modifying the Seshadri formula [1] for the flame velocity,

$$S_{L.d} = \frac{1}{Ze}\sqrt{\frac{2Bk_u}{\rho_u C_T}\exp\left(-\frac{E_a}{R_u T_f}\right)}, \qquad Ze = \frac{E_a\left(T_f - T_u\right)}{R_u T_f^2}, \qquad (4.2.2)$$

where E_a is the activation energy, Ze the Zeldovich number, and C_T the total heat capacity of the mixture, which includes the dust term inside, and can be calculated as

$$C_T = C_p + C_s \frac{4\pi r_s^3}{3}\frac{\rho_s}{\rho} n_s, \qquad (4.2.3)$$

where C_p is the heat capacity of gas, C_s the heat capacity of particles and ρ the density of the mixture, which can be expressed as $\rho = \rho_u + c_s$, where ρ_u is density of gas and c_s is the concentration of particles; $n_s = (c_s / \rho_s)/V_s = 3(c_s / \rho_s)/4\pi r_s^3$ is the amount of dust particles per unit volume.

As a separate component of the computational platform, we developed a numerical explosion venting analyzer (EVA) for the sake of evaluating burning processes occurring in vented enclosures. Unlike comprehensive CFD codes that always require signification computational facilities and time, the EVA is a very fast solver, which is simple to learn, use and extend further.

4.3. Experimental Platform to Measure *Laminar* Burning Rates of Dust-Gas-Air Mixtures

Figure 4.3.1(a) presents the schematic of the experiment setup used for the measurement of laminar burning velocity and dust entrainment rate. The design is based on the concept of a Bunsen burner having side openings to entrain coal dust particles in to the flow of the reactant mixture. Specific details of the dust injector in such a burner are discussed by Xie et al. [1]. The burner is made of a steel tube with an inner diameter of 10.2 mm and wall thickness of 1.2 mm. A 1 mm thick acrylic plate with a 1 mm diameter orifice is installed inside the steel tube, 150 mm away from the burner exit, to allow the flow streamlines to become parallel well before the burner exit. Dust is fed to the orifice plate through three openings of dimensions 7.5 mm wide and 9 mm long, located on the tube in an axisymmetric fashion above the orifice plate as shown in Fig. 4.3.1(b). A brass jacket tube of inner diameter 0.1 mm larger than the outer diameter of the steel tube is secured by two socket head screws. This is used to adjust the opening size and therefore the dust entrainment. Pittsburgh seam coal dust (with no additives) is used in the present study. Few separate experiments have been carried out with sand particles as well. The sand-dust particles are used to analyze the influence of an inert on the burning velocity. The coal dust is filled in an inverted cone-shaped acrylic container, which is also attached to the steel tube. The cone angle of the container is equal to 60°, which represent the critical angle of repose of dust particle size ranges used in this study. The repose angle is determined using an experimental method discussed by Botz et al. [2]. The adjustable burner and its attachments are secured in a support frame and the entire assembly is kept over a *Cole-Palmer Symmetry PR 4200* load cell. The load cell has a total weighing capacity of 4.2 kg with a sensitivity of 0.01 g. The factory specified uncertainty in the mass measurement is ± 0.03 g. A ring stand is kept outside the load cell to support a collection pan as shown in Fig. 4.3.1. Pittsburgh seam bituminous coal dust with particle sizes in the range of 0 to 25 μm, 53 to 63 μm, and 75 to 90 μm are used in the experiment. The size ranges are obtained by *Retsch AS 300* sieve shaker. Compressed air and methane (99.99% purity) cylinders are used to supply the burner with an upstream pressure of 0.5 bar. Each gas flow is controlled by a *SIERRA* Model 100 mass flow controller, which has an accuracy of ±1% of its maximum flow capacity.

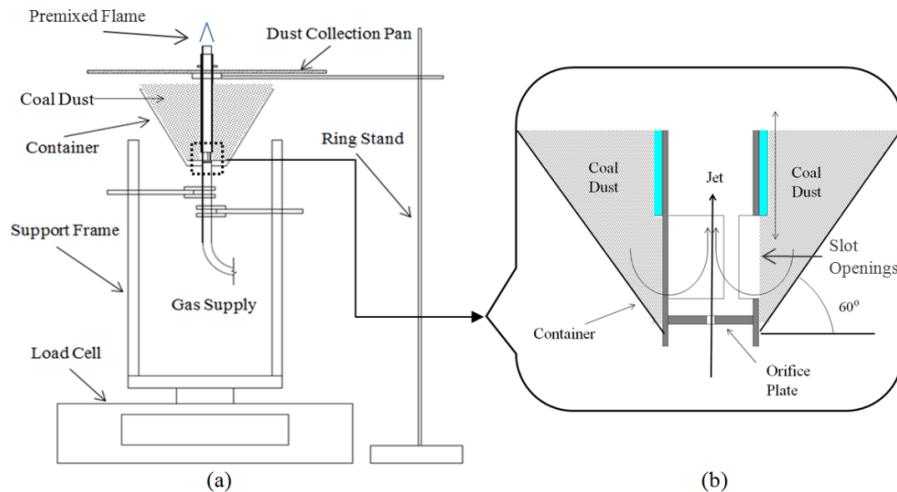(a)   (b)

6

Figure 4.3.1: Schematic of the experimental apparatus:
(a) dust burner and the weighing assembly; (b) dust entrainment assembly.

Direct shadowgraph technique is used to capture the flame cone with or without coal dust injection. The schematic of the shadowgraph setup is shown in Fig. 4.3.2. A projector lamp of capacity 420 W is converted into a point light source and placed at a distance of one focal length from a double convex lens. A Canon EOS 5D single-lens reflex (SLR) camera with a macro-lens (Canon EF100/2.8 Macro USM) with a minimum focal length of 31 mm is placed behind the flame along the center axis of the parallel light beam. The camera is manually adjusted (shutter speed: 1/4000 sec, ISO: 1600, aperture: 2.8) to obtain the sharpest image for post processing.
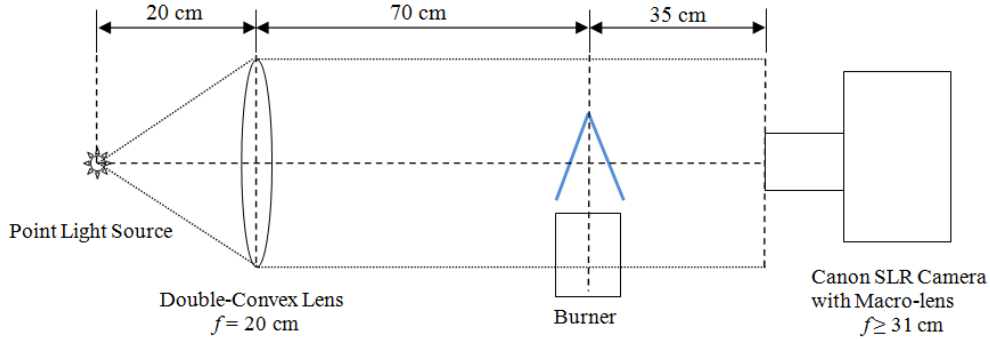

Figure 4.3.2: Schematic for shadowgraph setup.

4.4. Experimental Platform to Measure *Turbulent* Burning Rates of Dust-Gas-Air Mixtures

The primary objective of the experimental component of Phase II of this project was study to develop an experimental platform to accurately measure the turbulent burning velocity of a dust-gas-air flame with the capability of systematic variation of the key parameters such as particle size, dust type, turbulent intensity, integral length scale, dust concentration, and gas phase equivalence ratio. To accomplish these goals a new instrument called a *Hybrid Flame Analyzer* (HFA) was designed, instrumented, and constructed during this study. This instrument can control the laminar burning velocity (S_L), turbulent intensity (U_{rms}), and length scale (l_0) along with the particle size (d_{st}) and concentration (λ_{st}) of condense phase fuel to provide a measure of the burning velocity of gas, dust, or hybrid flames. The HFA is divided into several sections: combustion chamber, exhaust system, burner nozzles, dust feeder, and optical setup which are described below.

4.4.1. Combustion Chamber

The HFA's combustion chamber is used to contain the dust and ash generated and minimizes ambient air disturbances. Figures 4.3.1a and b show the details of the combustion chamber. The external frame (a) is made out of 3.81 cm angle aluminum 0.3175 cm thick. The external dimensions of the frame are 44 cm tall and 17.8 cm (wide. The frame is held together using #8-32 bolts with Loctite to prevent the nuts from coming loose over time. The edges of the frame were sealed using a high temperature RTV gasket maker (Permatex). Two of the walls were made of plate glass (b) 25.4 cm tall, 20.32 cm wide, and 0.238 cm thick. Rubber gasket 0.159 cm thick is used between the glass and the aluminum to prevent leaks and help prevent the glass from cracking. The glass was held onto the aluminum frame by eight tabs, two on each side.

The combustion chamber is divided into two sections, the main section with the burner and a small section at the bottom (c) 7.62 cm high where the makeup air is injected and allowed to disperse. Air enters the combustion chamber through hundreds of 0.159 cm holes drilled into a 28 guage steel plate which separates the section (d) similar to the experiment used in Bradley et

al. [3]. The makeup air is controlled using a flowmeter. During tests, 30 lpm of air is injected into the combustion chamber by a 0.635 cm Swagelok female tube adapter (e). The air is distributed through a 1.27 cm copper tube (not shown) with 1 inch wide slits cut into the side to help distribute the air in the lower section. The cooling water is injected and removed through two 0.635 cm Swagelok female tube adapters (f). The fuel for the burner pilot flame is injected into the combustion chamber through another 0.635 cm Swagelok female tube adapter (g). The third side of the combustion chamber is made of a plate of 28 guage galvanized steel plate (i). The water cooling fittings (f), pilot fuel gas (i), a biconvex lens (h), and the spark igniter (j) are connected through this steel plate and sealed with high temperature RTV gasket maker. The optics system uses two bi-convex lenses (h), which are attached to the combustion chamber. The spark igniter (j) is mounted on a 30.48 cm aluminum rod surrounded by rubber housing. This housing allows the igniter to be moved inside of the combustion chamber allowing it to ignite the pilot and then be moved out of the way. The 4th side of the combustion chamber is a door (l) to access the inside of the combustion chamber. This door is composed of 0.3175cm (1/8") thick aluminum frame with a 25.4 by 20.32 cm by 0.238 cm plate glass allowing to see inside the combustion chamber. The door was attached to the main aluminum frame using a one-piece door hinge. EPDM rubber weather sealing, 0.794 cm and 1.51 cm wide, is used to seal the door. Pressure clamps (not shown) are used to hold the door closed during testing. The top of the combustion chamber contains a fume hood (m) to remove combustion products.
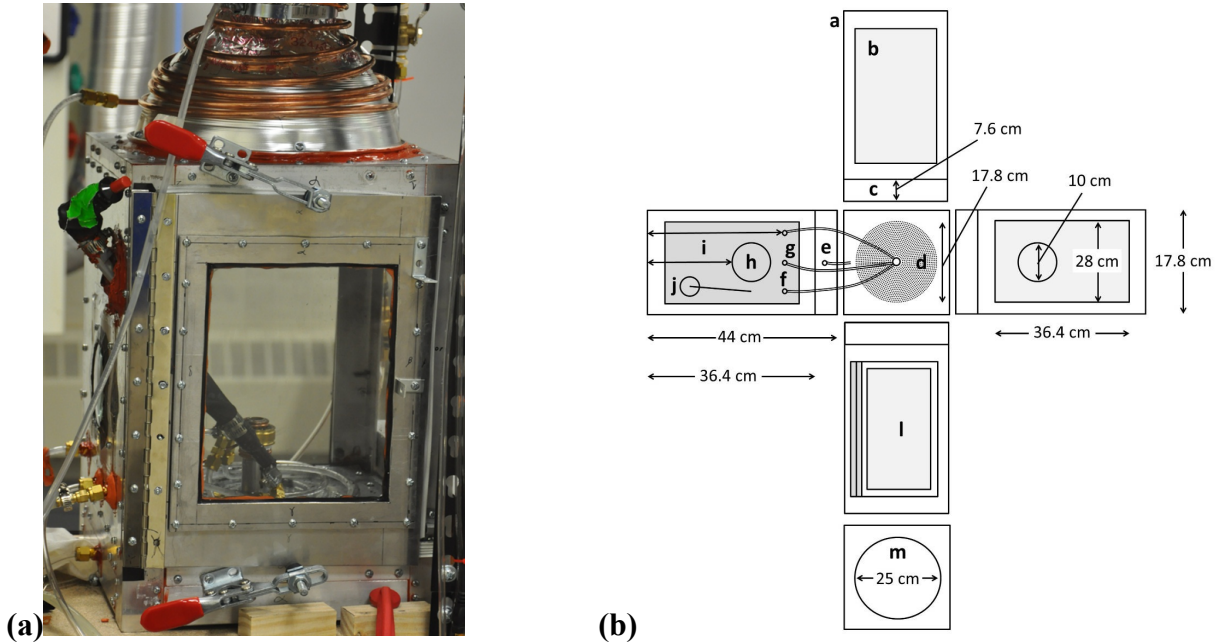

Figure 4.3.2: Image (a) and exploded view (b) of the Hybrid Flame Analyzer (HFA) combustion chamber.

4.4.2. Exhaust System and Burner Test Section.

The HFA exhaust system is shown in Fig. 4.3.3a. The combustion products are removed from the combustion chamber through the water cooled fume hood. The water cooled tubing (not shown) consists of 0.635cm OD copper tubing wrapped around the aluminum hood. Water flows at a rate of 10 lpm. The combustion products are pulled into exhaust tubing by a centrifugal pump. To help cool the exhaust products and prevent any pressure differential in the combustion chamber, excess air is pulled into the exhaust ducting through a makeup air system. The makeup

air ducting contains an s-bend to prevent hot combustion products from escaping into the laboratory. The cooled combustion products are exhausted out of the lab through more 10.16 cm (4") diameter tubing. The flow through the exhaust system is 0.0178 m^3/s (1068 lpm).
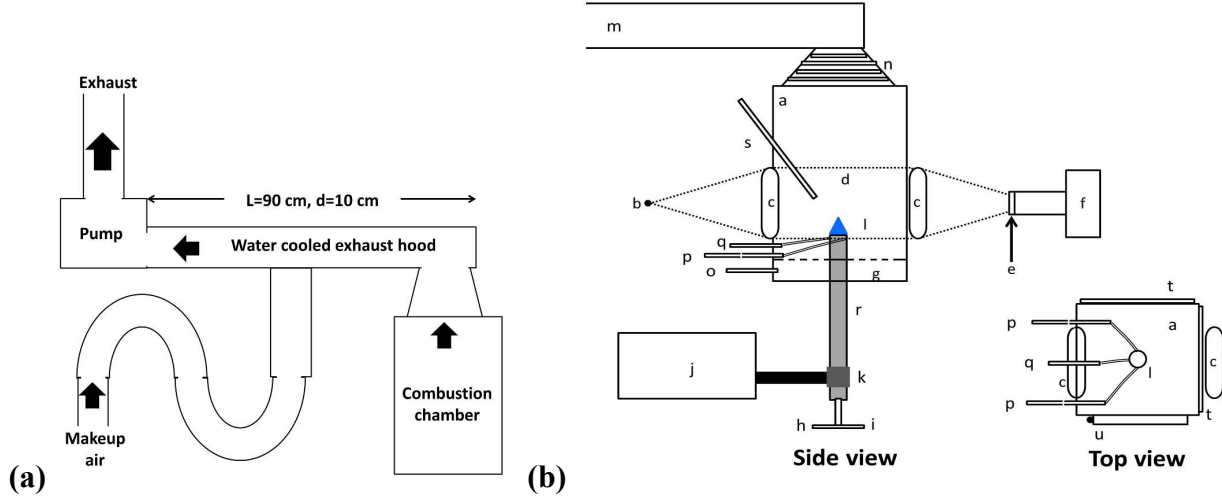

Figure 4.3.3: The diagrams of the HFA exhaust system (a) and the entire test section (b).

To determine the best way to study hybrid flames, a literature search for published methods of experimental burning velocity measurements of flames was conducted. Based on this study and the critical reviews by Andrews et al. [4] and Lewis & Elbe [5], the anchored Bunsen burner experimental design used in this work was chosen. This style of experiment is the simplest to use and analyze, and allows a turbulent flame which can be studied for an extended period of time facilitating easier instrumentation and measurement accuracy. This is needed because turbulent flames are inherently not steady; therefore, average quantities determined about the flame should come from many measurements taken over time. This requires a flame front to be anchored at the burner exit for several minutes.

Figure 4.3.3b shows a diagram of the hybrid flame analyzer's test section. The side view and top view of the combustion chamber are shown: the outline of combustion chamber (a), the point source of light (b) uses a bulb from a projector (480 watt). A steel plate with a pin hole in the center is used to create the point source. This point source of light is placed at the focal point of a bi-convex lens (b) with a 100 mm diameter and a 200 mm focal length. This creates a 100 mm diameter test section of parallel light (d) inside the combustion chamber. The parallel light passes through the flame (l) and through a second identical bi-convex lens which reduces the diameter of the image. This reduction makes the image small enough to fit on the sensor of a digital single reflective lens camera with a 1-1 macro lens (f) with the focus set to infinity. To reduce the intensity of the coal dust emissions, a short pass filter (e) with a cutoff of 550 nm is placed in front of the camera lens, similar to the experiment by Goroshin et al. [6]. The flame (l) is fueled from a methane source (h), an air source (i), and a dust hopper (j). Desired turbulent intensities are created using a set of perforated plates as described below. Makeup air is injected into the combustion chamber through the 6.3 mm fitting (o) and distributed in the subsection of the combustion chamber (g). The combustion products are removed from the water-cooled (n) 12 cm diameter exhaust duct. A removable spark igniter (s) is used to ignite the pilot flame, similar to the experiment used by Bradley et al. [3].

9

4.4.3. Burner Nozzle Design

At the top of the vertical feeder tube two different water cooled nozzles, with internal diameters of 14.5 mm, are attached to the top of the feeder tube as shown in Fig. 4.3.4. The first nozzle (a) is a straight tube used for creating laminar flames. Laminar flames are generated using a combined air-methane flow rate of 10 lpm. The second nozzle (b) uses a set of perforated plates to generate turbulence and has a methane-oxygen annular pilot to anchor the flame.

The details of construction of the turbulent burner nozzle are illustrated in Figs. 4.3.5. The turbulent flame (a) fueled by the dust air mixture (j) is anchored to the burner nozzle using a methane oxygen pilot flame (b). The nozzle tip is water cooled using 1/8 in copper tubing (c). The pilot flame fuel air mixture (e) is injected through pilot fuel housing (d) with a 0.635 cm Swagelok tube to MNPT fitting (not shown). The stainless steel housing (g) with an internal diameter (l) of 14.5 mm was cooled using 0.318cm copper tubing (f) similar to Bradley et al. [3] and Kobayashi et al. [7]. Turbulence is generated by nylon perforated plates (h) mounted 10-30 mm from the nozzle exit (k), shown in Fig. 4.3.6. The pilot flame housing (shown in a close-up view) is made up of three sequential copper tubes. The inner tube (g) has the same inner diameter as the stainless steel tube (g) and is 0.036 cm thick. The 2nd tube (o) is an insert which both creates the uniform high speed flow around the radius of the burner and maintains the constant spacing of the third tube (q), attached to the pilot fuel housing. This insert (o) is 0.071 cm thick and has 8 vertical slots cut into the inside (p) 0.127 cm deep. The top of the insert was machined on a lathe to create a double notch at the top. The deeper notch (n) allows gas to distribute around the circumference of the tube evenly and is approximately 0.254 cm deep. The second notch (m) creates an anchored methane-oxygen flame and is approximately 0.127 cm deep.
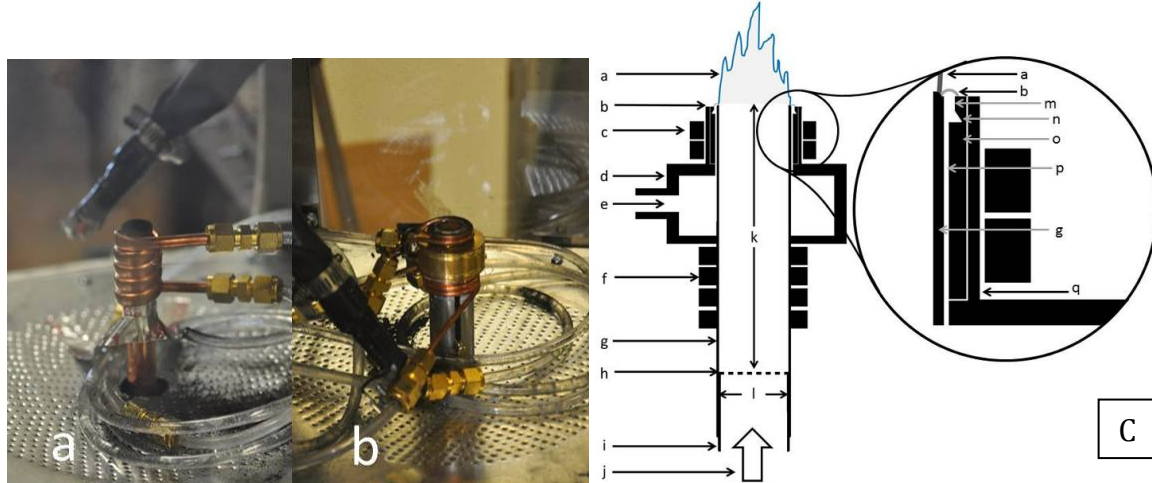

Figure 4.3.4: Images of (a) laminar and (b) turbulent nozzles and a (c) diagram of a turbulent nozzle.
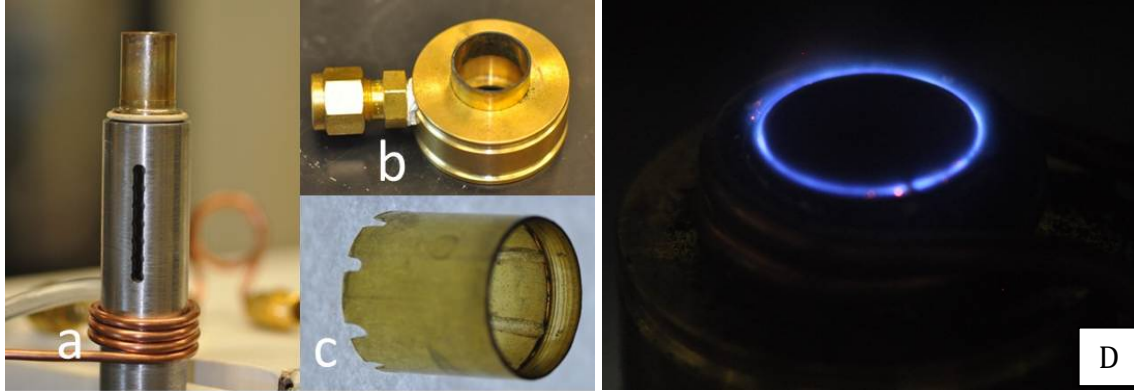
Figure 4.3.5: Turbulent burner parts: (a) side view of turbulent burner without pilot gas fitting (b) a pilot flame gas fitting (c) a pilot flame spacing insert; (d): image of a premixed methane-oxygen pilot flame.

Figure 4.3.5 (a-c) show images of the individual components in the turbulent burner nozzle. Namely, Fig. 4.3.5a shows a side view of the main burner tube without the pilot flame assembly or water cooling; Fig. 4.3.5b presents the fitting which allows the pilot fuel gas to be added and evenly distributed around the circumference; Fig. 4.3.5c shows the spacing insert which keeps the spacing of the pilot gap constant around the circumference and increases the velocity of the oxygen-methane mixture. Eventually, Fig. 4.3.6 shows the images of the perforated plates used in this work. Five perforated plates were created having various hole diameters: 4mm (a), 3mm (b), 2mm (c), 1mm (d), and 0.6mm (e). These round perforated plates are similar to that used by Khramtsov

Figure 4.3.6: Perforated plates.

[8]. The perforated plates are mounted in identical nylon tubes (f) which have a threaded hole for the adjusting pin. The 1 mm perforated plate has a blockage ratio (area of holes/total area) of 50%. The annular pilot, shown in Fig. 4.3.5d, is similar to the one used by Kobayashi et al. [7]. It is necessary to hold the flame due to the high flow rates used to generate turbulent intensity and is fueled by methane and oxygen mixture ($\phi = 1$). This mixture was used because of the higher burning velocity, which (as compared to air) prevents the turbulence in the main burner flow from disturbing the pilot. Both burner nozzles have water cooling (10 liters per hour controlled by a flowmeter) made out of copper tubing wound around a burner diameter with thermal grease (Arctic Silver Ceramique Thermal Compound) to raise conductive heat transfer.
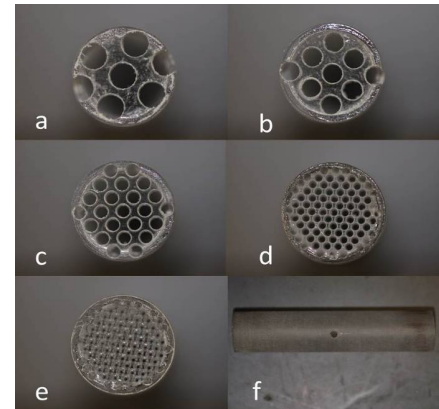
The main burner flow has been measured using a hot wire anemometer (Dantec Dynamic 9055P011), sampling at a rate of 100 kHz. The platinum-plated tungsten wire sensor has a diameter of 5 microns and is 1.25 mm long. The hot wire anemometer was calibrated using the average bulk flow velocity through the burner based on the mass flow controller. The calibration curve follows a power law relationship as shown in Fig. 4.3.7.
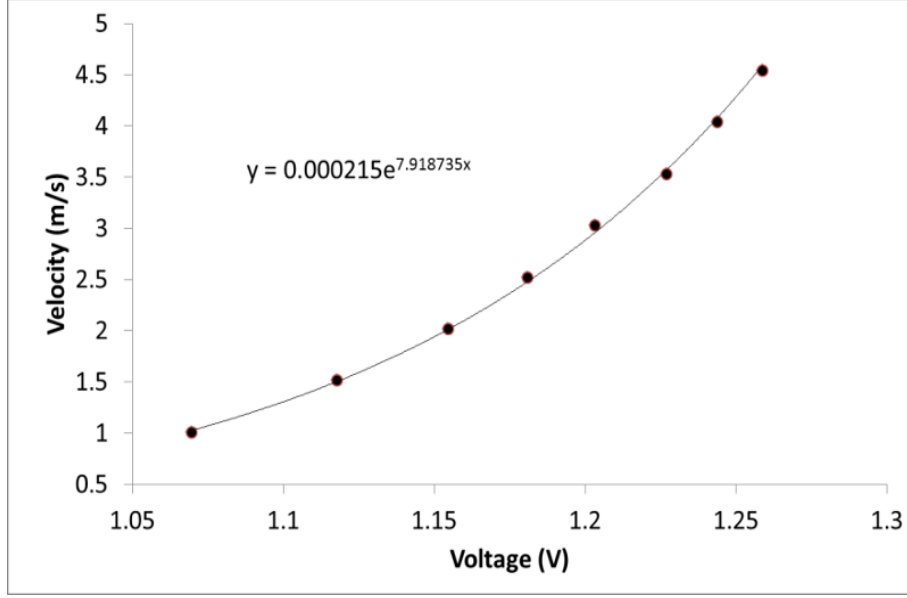
Figure 4.3.7: Calibration curve for hot wire anemometer.

A turbulent flow is described in a standard way as

$$u = \bar{u} + u' \, ,$$

(4.3.1)

where u is the flow velocity, $\bar{u}$ is the average flow velocity, and u' is the fluctuating component of the flow velocity. The turbulent intensity is defined as the root mean square (RMS) of the turbulent fluctuation in the u', i.e.

$$u'_{rms} = \sqrt{\frac{\left(u'_1\right)^2 + \left(u'_2\right)^2 + ... + \left(u'_n\right)^2}{n}} \ .$$

(4.3.2)

The velocity measurements in the experiments described below are done in cold flow without a flame similar to Kobayashi et al. [7]. Pope [9] discussed how the flame could have an effect on the turbulent velocity field due to the large temperature rise of the flame, but with few exceptions, these effects have not been studied. However, Chomiak [10] found that a wrinkled, continuous laminar flame does not generate additional turbulence and actually reduces the overall intensity of the turbulent velocity fluctuations. The use of perforated plates, as discussed below, has been shown to be a reliable way to produce predictable turbulence intensities. In the HFA, the turbulence intensity is controlled with the flow rate through the burner and the distance of the perforated plate from the burner exit. Combined air-methane flow rates of up to 4 m/s are used to generate a range of turbulent intensities up to 0.532 m/s. Figure 4.3.8 shows the turbulent intensity generated as a function of perforated plate location and flow velocity. Positions 1, 3, and 6 (as shown in Fig 4.3.5a as the notches in the side of the slit, the first notch is covered by water cooling tubing and is not used) are located 10, 15, and 30 mm below the nozzle exit, respectively. The red dots in Fig. 4.3.8 indicate the perforated plate location and flow velocity range used in the current study. This set of conditions was chosen because it matched the turbulent intensities used by Kobayashi et al. [7] and further, when the 1mm perforated plate was raised to position 3, the flame flashed back inside of the burner. Due to time constraints, all of the possible perforated plate and flow rate combinations were not tried with a flame to determine

12

which combinations had a stable condition. The turbulent integral length scale l_0 is

$$l_0 = \bar{u} \int_0^\infty \rho_u(\tau) d\tau ,$$

(4.3.3)

where $\rho_u(\tau)$ is the autocorrelation of the velocity fluctuation u'.
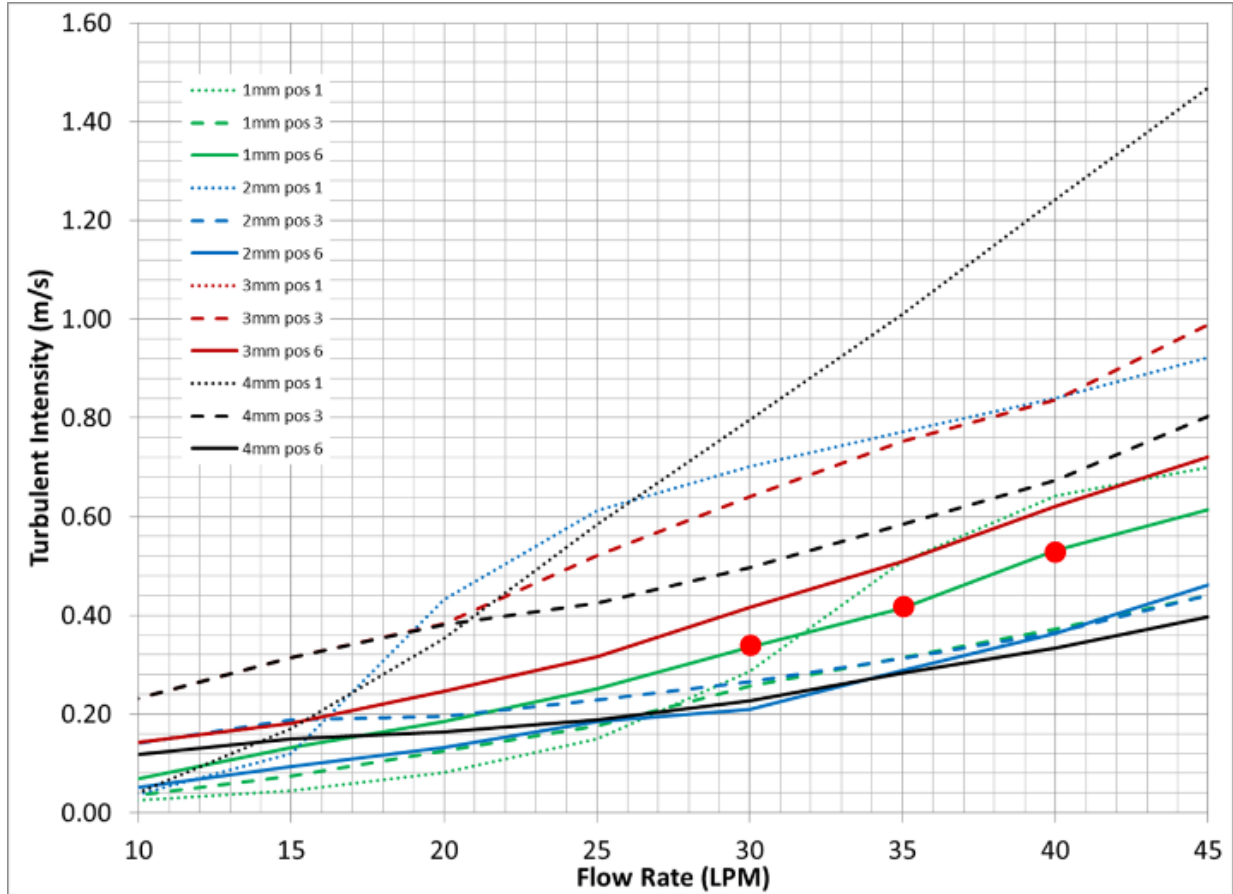

Figure 4.3.8: Turbulent intensity versus flow rate.

5.0 SUMMARY OF ACCOMPLISHMENTS AND INNOVATION HIGHLIGHTS

5.1. Products and Dissemination

The project outcomes are published and submitted for publication in refereed journals, and they were and will be disseminated in the form of conference presentations at various international, national and regional meetings, including the 35th International Symposium on Combustion (San Francisco, Aug 3-8, 2014); the 31st & 32nd International Pittsburgh Coal Conferences (Pittsburgh, PA, Oct 6-9, 2014 & Oct 5-8, 2015); the 40th AIAA Dayton-Cincinnati Aerospace Sciences Symposium (Dayton, Mar 4, 2015); the 90th West Virginia Academy of Science Annual Meeting (West Liberty, Apr 11, 2015); the High Performance Computing Meeting (Morgantown, Apr 16 2015); the 9th US National Combustion Meeting (Cincinnati, May 17-20, 2015); and the ASME Power Conference (San Diego, June 28 - July 2, 2015). All these manuscripts are attached among appendices. Some of these conference papers and poster presentations have won prizes.

Overall, a total of 15 products have been generated during the project period, namely:
1. 3 peer reviewed journal papers (one published; one under review; one to be submitted)

2. 10 Conference papers (International Combustion Symposium; International Pittsburgh Coal Conference; National Combustion Meeting; ; AIAA, ASME, & WVAS)
3. 1 poster
4. 1 MS thesis

5.2. Analytic Accomplishments (Predictive Scenario)

Partial formulations on the Darrius-Landau flame instability by Akkerman et al. [12] and that on the finger flame acceleration by Bychkov et al. [13] were combined. We have started with a homogenously-gaseous environment and then incorporated the effects of combustible and inert dust particles by means of the Seshadri formulation [1]. Due to the difference between the axial and radial flame-generated flows in a tunnel/channel, at a certain time, t_{sph}, a globally-spherical, cellular flame front acquires a finger-like shape and accelerates faster. While the finger acceleration is very strong, it lasts for a short time only, $t_{sph} < t < t_{wall}$, until the flame skirt contacts the passage wall at a certain instant t_{wall}. The quantities t_{sph} and t_{wall} versus the equivalence ratio are shown in Fig. 5.1.1 for methane-air and propane-air flames. Figure 5.1.2 presents the time evolution of the flame tip position and its velocity. The maximum quantities attained are shown in Fig. 5.1.3 versus the equivalence ratio. For a comparison purpose, we also used propane parameters along with that of methane in the plots.
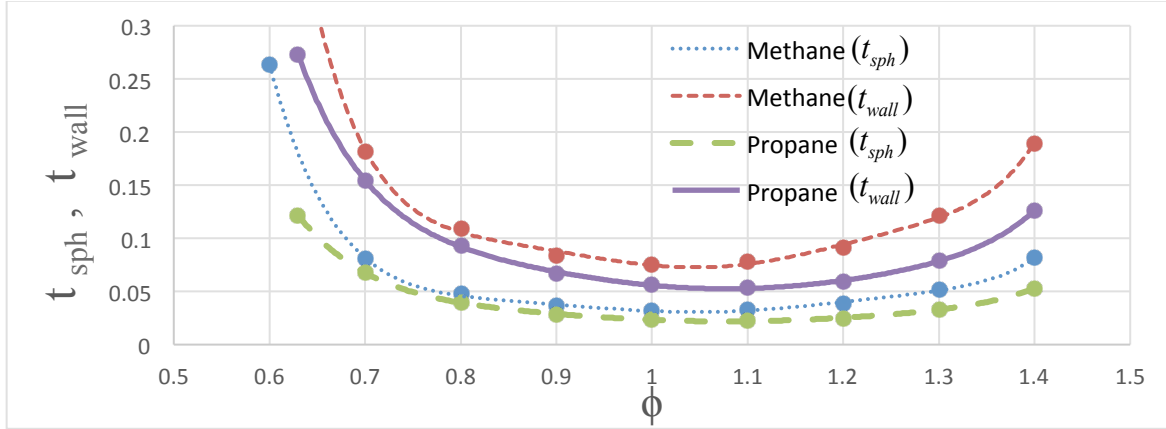

Fig. 5.1.1: The time limitations of the finger flame acceleration, t_{sph} and t_{wall}, versus the equivalence ratio ϕ for propane-air and methane-air flames in a mine tunnel of width 1m.
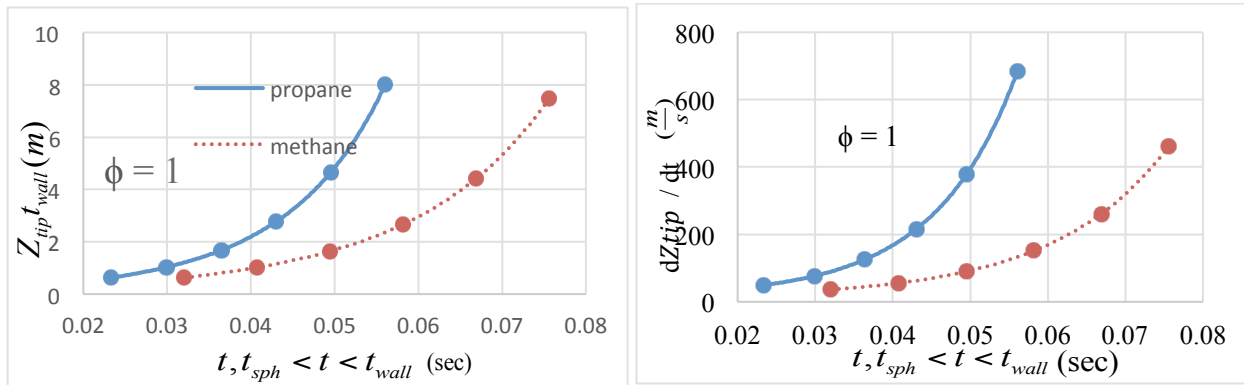

Fig. 5.1.2: Evolution of the flame tip position and velocity in a stoichiometric mixture.
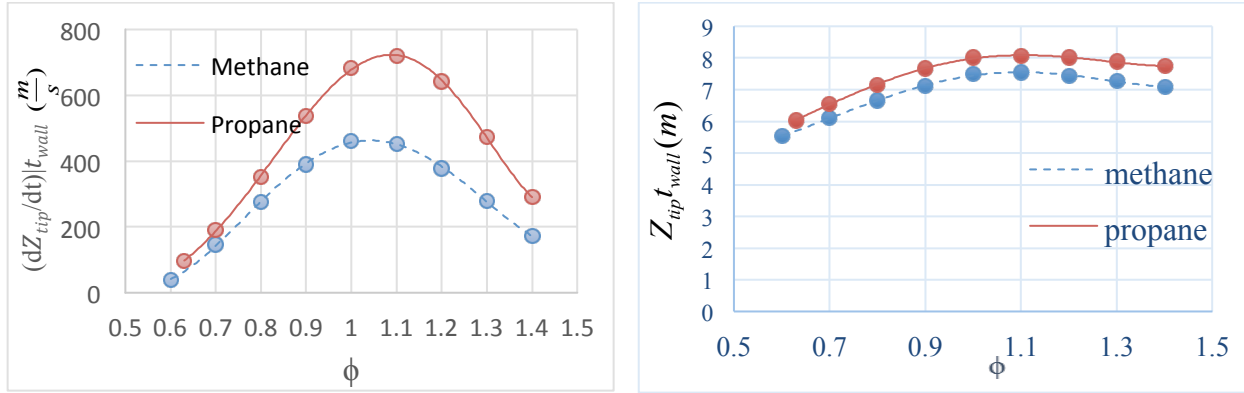
14

Fig. 5.1.3: Maximal methane-air and propane-air flame tip velocity and position versus ϕ.

A convenient and conventional parameter to analyze the flame acceleration in the DDT process is the so-called *flame run-up distance* (r.u.d.) – a distance that a flame front propagates from its ignition to the detonation initiation. In fact, two distinct definitions of the r.u.d. are frequently employed in the DDT studies, namely (i) as a distance that a flame front propagates from its ignition to the detonation initiation; or (ii) as a distance, at which the flame propagation velocity in the laboratory reference frame attains the sound speed. In a similar way one may also define the *run-up time* as the instance when the flame speed in the laboratory reference frame penetrates the sound barrier. While in the former case (i) the run-up distance depends strongly on a particular chemical kinetic mechanism of the reactions involved, in contrast, in the latter case (ii) the r.u.d. is a purely gas dynamic characteristic of the process. This project is focused on the gas dynamics of the flame acceleration. For this reason, the second definition for the run-up distance has been employed. Namely, we approximated the r.u.d by the flame tip position at the instant when its velocity is equal to the local sound speed, $dZ_{tip}/dt = c_o$. The result is shown in Fig. 5.1.4 vs the equivalence ratio ϕ for methane-air and propane-air combustion. Comparison of Figs. 5.1.2–5.1.4 yield that for the equivalence ratios in the range of $0.9 < \phi < 1.2$, for methane-air mixtures, and that in the range of $0.8 < \phi < 1.3$, for propane-air ones the detonation can be triggered by the time t_{wall}.
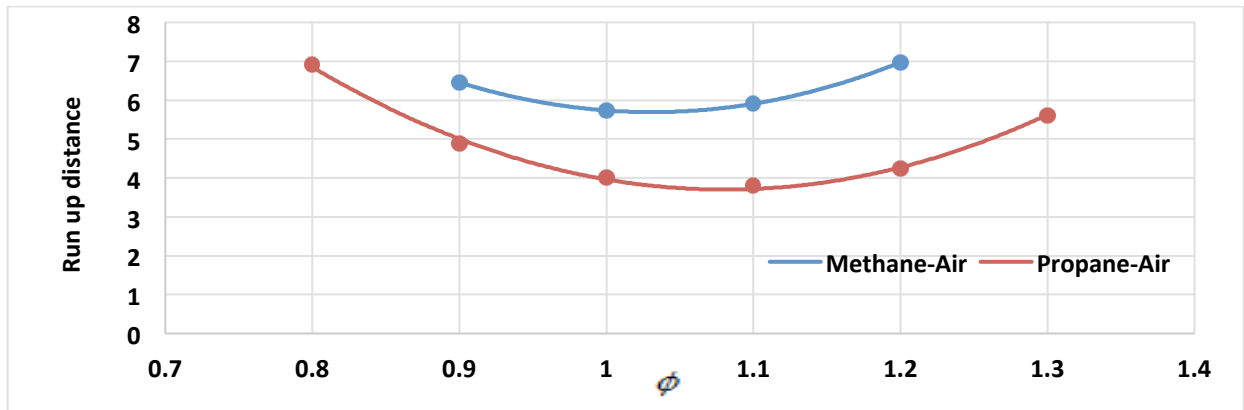

Fig 5.1.4: Flame run-up distance versus the methane-air / propane-air equivalence ratio.

Although figures 5.1.2–5.1.4 were limited to gaseous fires, the analysis has subsequently been extended to dusty-gaseous ones, with inert and combustible dust used. While inert particles (sayi.e. , sand) may mitigate the fire, the combustible (sayi.e. , coal) particles work vice versa.

Moreover, coal particles can release volatiles into the gaseous mixture. The volatiles are the additional component of the gaseous fuel, which increases the local equivalence ratio and elevates the flame temperature, thereby widening the explosivity limits and promoting the flame speed. Figures 5.1.5 and 5.1.6 are the counterparts of Figs. 5.1.1 and 5.1.2, showing how combustible or inert particles influence the fire characteristics (the timing, the flame locus and velocity as well as the flame run-dup distance) depending on the dust particle size and concentration. Overall, it is demonstrated that for near-stoichiometric, methane-air/dust combustion $(0.8 < \phi < 1.3)$ the overall acceleration scenario may promote the flame velocity by two orders of magnitude, up to supersonic values. In addition to the direct disaster of such a fast fire, this may facilitate the DDT, thereby leading to additional hazard (shocks) to the mining personal/equipment. More details are presented in Appendices attached.
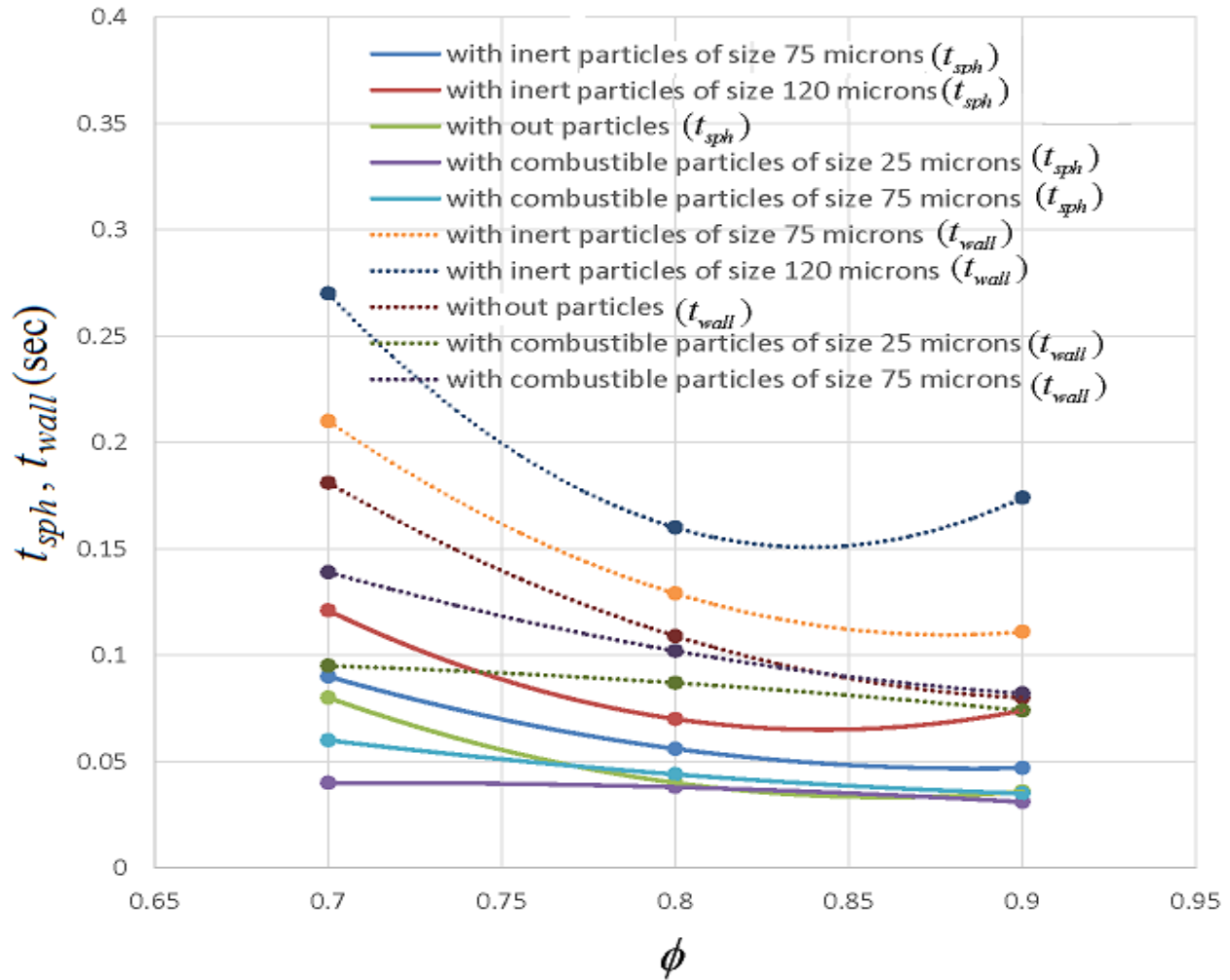

Fig. 5.1.5: The time limitations of the finger flame acceleration, t_{sph} and t_{wall} , versus the equivalence ratio ϕ for methane-air-dust flames in a mine tunnel of width 1m.
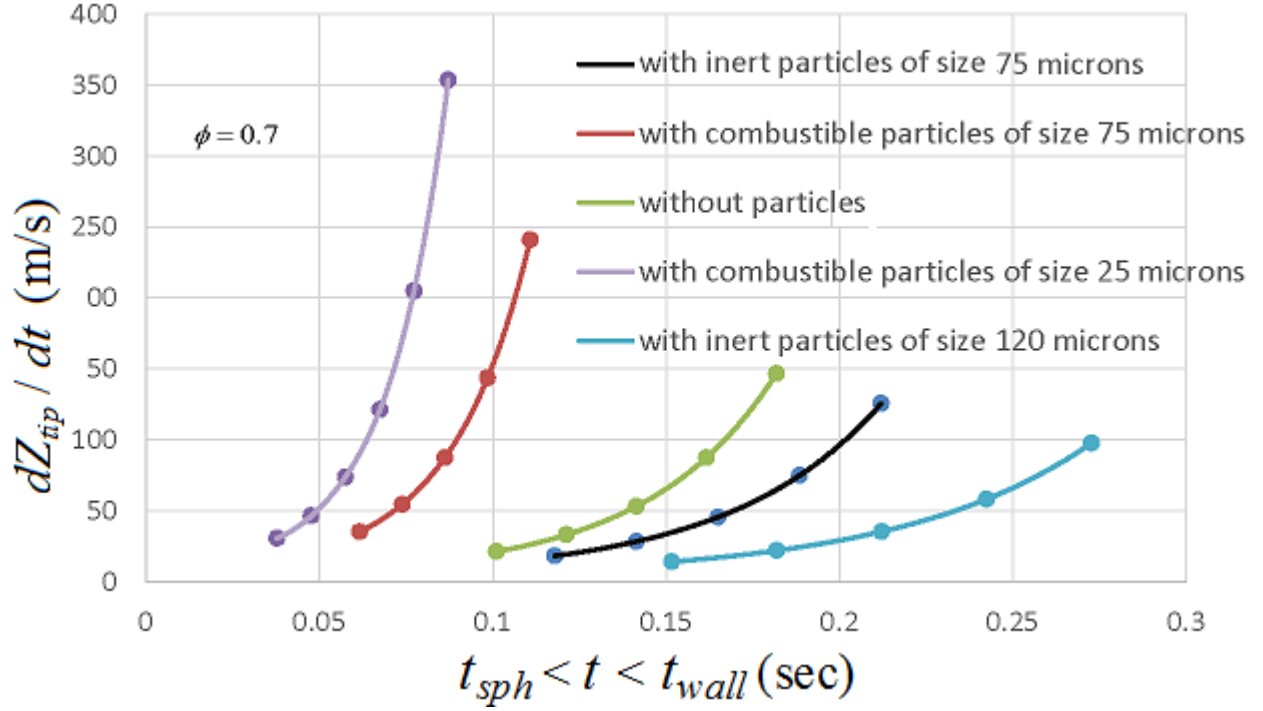
16

Fig 5.1.6: Effect of combustible and inert dust on the evolution of the flame tip velocity.

5.3. Computational Accomplishments (GEM and D-GEM)

The computational platform has been developed and tested by means of considering various noncombustible dust distribution gradients to investigate the effect of dust particles on the flame evaluation as shown in Figs. 5.2.1–5.2.4. First consideration is the uniform dust distribution, where dust particles spread with equal number and distance to each other along the tube. Second, we consider non-uniform dust distribution along the tube as a function of tube radius in radial direction. Within the non-uniform dust distributions, we investigate the effect of different dust distribution gradients such as linear, hyperbolic and parabolic functions on the planar flame speed and flame acceleration. In the case of linear dust distribution as shown in Fig.5.2.1 (b), we consider bottom of the tube that has maximum amount of dust particles, n_{max}, and top of the tube there is no dust particles. By applying the boundary conditions on the linear gradient of non-uniform dust distribution, we end up with a function of the tube position,

$$n_s = \frac{n_{max}}{2}\left(1 + \frac{x}{R}\right). \tag{5.2.1}$$

In the case of a uniform dust distribution, Fig.5.2.1, Eq. (5.2.1) obviously reads $n_s = n_{max}/2$. Additionally, for the linear case we also consider dust distribution at the different angles that is shown with $\emptyset$, in the other words we change the dust particles numbers at the top of the tube from zero to n_{max} and take bottom of the tube at constant amount of dust which is n_{max}. Related equation can be given as below where $\emptyset$ differs between $0 \le 0.3n_{max}, 0.7n_{max} \le 1.0n_{max}$:

$$n_s = n_{max} + \frac{n_{max} - \emptyset}{2R}(x - R). \tag{5.2.2}$$

Then we considered the case of tangential hyperbolic dust distribution where a is a constant. In this case dust distribution is maximum along bottom and top of the tube and zero along the axis.

17

$$n_s = n_{max}\left(\frac{\tanh\left(a(x/R)^2\right)}{\tanh(a)}\right). \tag{5.2.3}$$

Finally, we have considered a parabolic dust distribution, given by

$$n_s = n_{max}\left(\frac{x^2}{R^2}\right). \tag{5.2.4}$$

This case looks like similar with the tangential hyperbolic dust distribution except for its natural characteristic behavior.
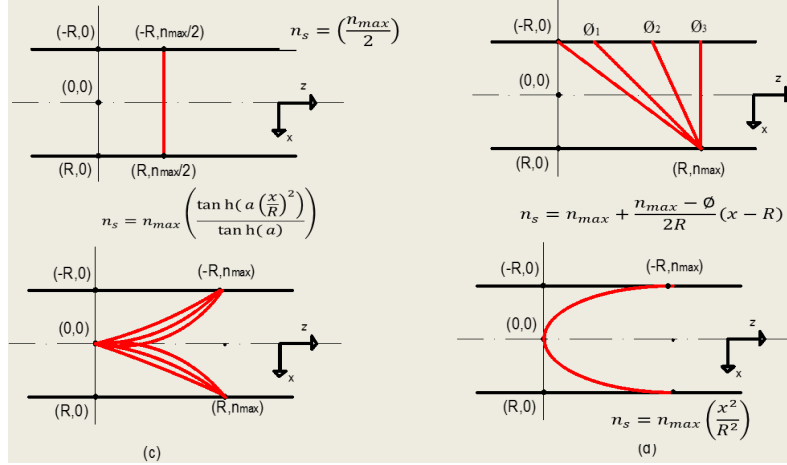

Fig.5.2.1: (a) Homogenous dust concentration distribution; (b) Linear dust concentration distribution with different distribution angles, where $\emptyset_1 = 0.3\ n_{max}$, $\emptyset_2 = 0.7 n_{max}$ and $\emptyset_3 = 1.0 n_{max}$; (c) Tangent hyperbolic dust concentration distribution; (d) Parabolic dust distribution.
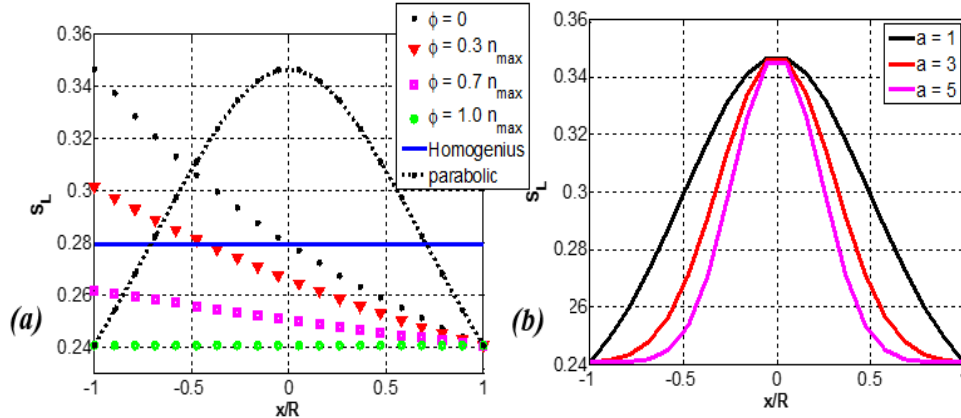
Fig. 5.2.2: Planar flame speed versus the scaled channel width:
(a) Homogenous, linear and parabolic dust cases; (b) Tangent hyperbolic case.

As a result, by solving governing equations with implemented dust particles, first, we can obtain S_L values within the channel for different dust distributions as shown in Fig. 5.2.2. In this project, we also visualize the complete evaluation of the flame for different dust distributions as shown in snapshots in Fig. 5.2.3, and the flame evaluation in sown in Fig. 5.2.4. We took the channel radius R = 25 L_f. Figure 5.2.5 shows the flame acceleration rate for various dust distribution gradients at the flame propagation Reynolds numbers, $\text{Re} = RS_L^{mean}/\nu = R/\text{Pr}\,L_f$.

Fig. 5.2.3: Flame front shape in channel of radius R = 25 L_f. The colors designate the temperature: from 300 K in the cold gas to 2400 K in the burnt matter.
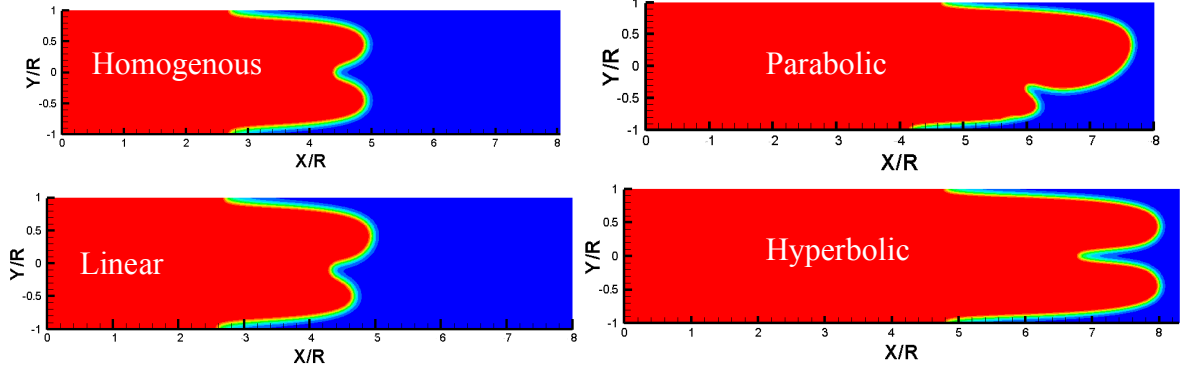(a) Homogenous dust concentration distribution;
(b) Linear dust concentration distribution for $\emptyset = 0$;
(c) Linear dust concentration distribution for $\emptyset = 0.3n_{max}$;
(d) Hyperbolic dust distribution; (e) Parabolic dust concentration distribution.
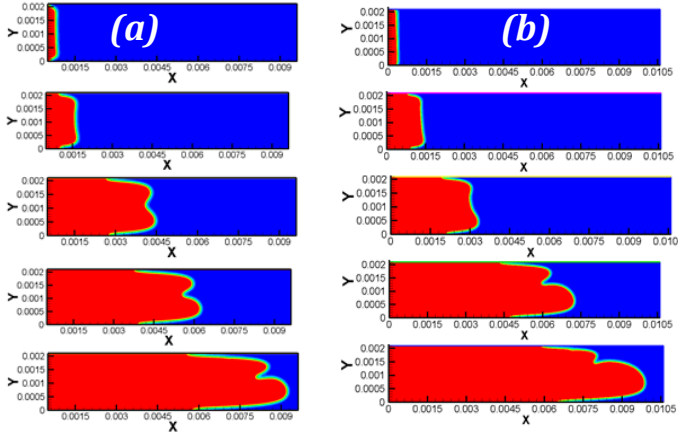
Fig. 5.2.4: Flame evaluation shape in channel of radius R = 25L_f. (a) Linear for $\emptyset = 0$; and (b) parabolic dust distribution.
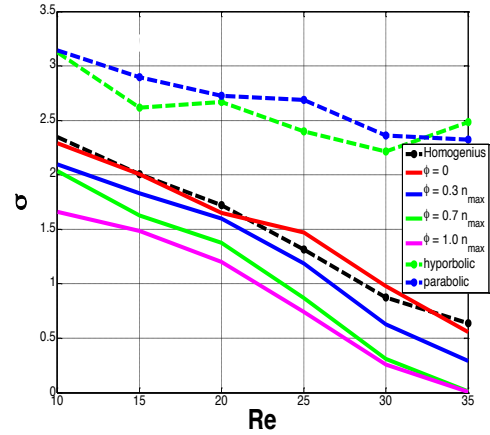
Fig. 5.2.5: The acceleration rate versus the flame propagation Reynolds number for various dust distribution gradients.

Eventually, turbulence has been incorporated into the computational platform by means of a sub-grid-scale (SGS) model for an "effective", turbulence-induced "planar" flame speed. So far, two models have been considered, namely

$$\frac{S_T}{S_L} = 1 + C\left(\frac{u'_{rms}}{S_L}\right)^n, \qquad (5.2.5)$$

and

$$S_T \Big/ S_L = \sqrt{Re_T}, \qquad Re_T = \frac{U_{rms}}{S_L}\frac{L}{L_f}. \qquad (5.2.6)$$

It is nevertheless noted that the platform is flexible with respect to the turbulence model such that any other model can readily be incorporated. Moreover,
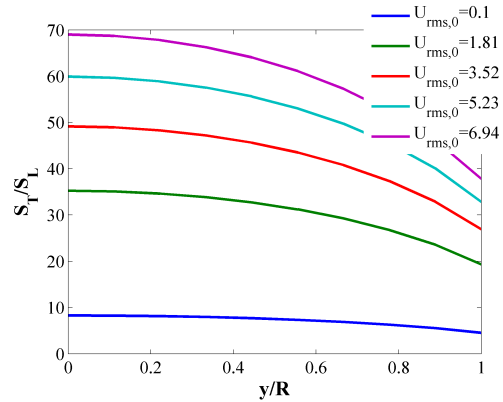
Figure 5.2.6: Turbulent flame velocity

variable in space and/or time the rms-velocities can be considered. So far, the following, parabolic space-distribution for the turbulence intensity has been employed as a test case

$$U_{rms} = U_{rms,0}\left(1 - A\frac{y^2}{R^2}\right),$$ (5.2.7)

with $0.1 \le U_{rms,0} \le 6.94$ m/s and $A = 0.7$. The result is shown in Fig. 5.2.6.

5.3.1. Explosion Venting Analyzer (EVA)

As a separate component of the computational platform, we developed a numerical explosion venting analyzer (EVA) for the sake of evaluating burning processes occurring in vented enclosures. The EVA is based on a fundamental approach, and it has already been employed towards a variety of enclosure shapes, dimensions and combustible gas concentrations. The EVA predictions agree well with a wide domain of experimental data, including the internal pressure evolution and the effect produced by the external explosion. To be specific, we have incorporated various flame velocity formulations as well as flame shape stretching produced by the venting and the thermal expansion restriction experienced at the vicinity of the walls. It is shown that inclusion of vents in the enclosures provides significant reduction on the peak overpressures, but in a less efficient way if the opening size is further increased (Fig. 5.2.7a). Moreover, the external explosion produced once the flame propagating internally reaches the vent, igniting the previously expelled gas, is responsible for the largest overpressure registered in the enclosure, as seen at the second peak of the trends in Fig. 5.2.7b.

(a)   **(b)**
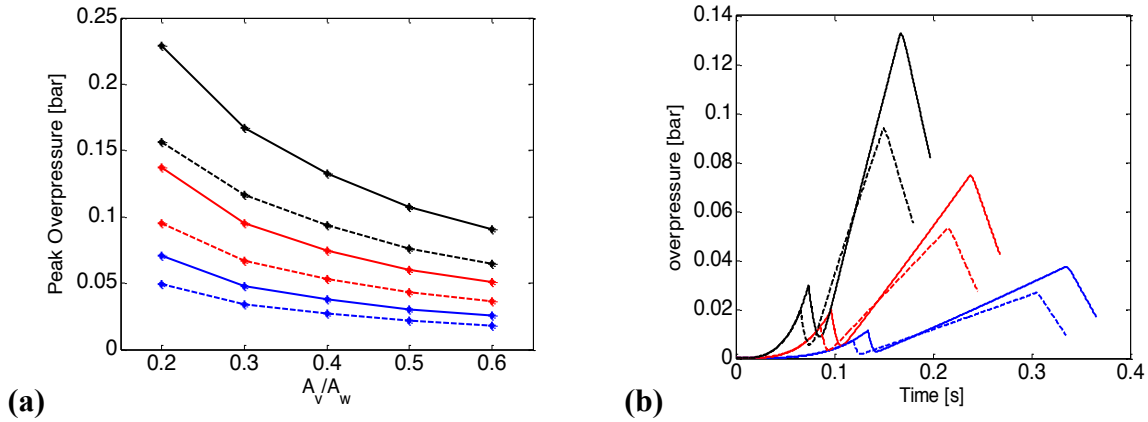
Fig. 5.2.7: Peak overpressures in a 63.5m³ cuboid enclosures: (a) at different vent to wall area ratios and (b) its time evolution. Scenarios varies with hydrogen concentrations 14% (blue), 16% (red) and 18% (black), rear (solid) and central ignition (dashed).

5.4. Experimental Accomplishments

A sample image of the actual flame and the shadowgraph image obtained by the macro-lens are shown in Fig. 5.3.1. The main advantage of the shadowgraph is that it can capture clearly the flame cone even when the flame is loaded with high concentration of burning particles. As seen in Fig. 5.3.1a, it is hard to locate the edge of the flame cone using conventional direct photograph technique, while the flame cone is easily identified in the shadowgraph (Fig. 5.3.2b).

| Actual Flame Image | Shadowgraph | Image in Matlab |
| (a) | (b) | (c) |
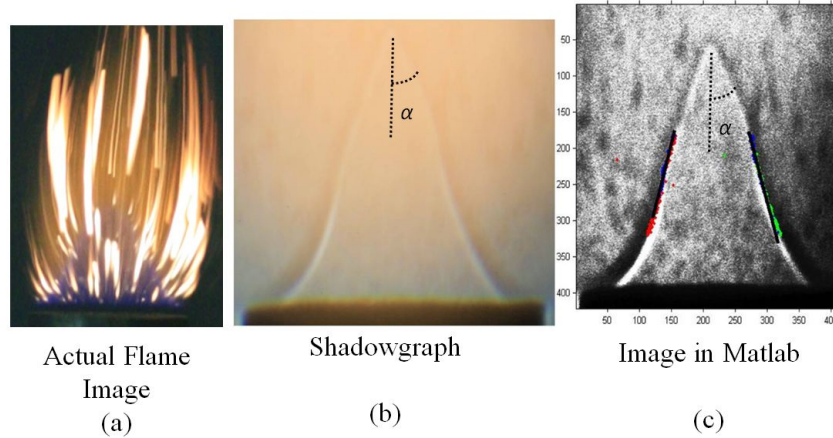
Figure 5.3.1: Photographs of (a) actual flame, (b) shadowgraph and (c) processed image.

For each dust concentration and equivalence ratio of the reactant mixture, a minimum of 15 images are captured and processed by an image process algorithm programed in MATLAB. The corresponding average cone angle is used to estimate the laminar burning velocity. A sample of the processed image is shown in Fig. 5.3.2c. The algorithm converts the shadowgraph into a gray-scale image and detects the cone edge where a significant change in the normalized intensity (a value from 0 to 1) is observed on each row within the preselected boundary of the flame cone. The detected cone edge is shown as two clusters of dots in Fig. 5.3.2c. Slopes that connect each dot on one side of the cone are calculated. Then a best-fit line for all the detected dots, shown as black solid line in Fig. 5.3.2c, is used to obtain the averaged cone half angle (α). The standard deviation of the angle experimentally measured is within ± 1.5°. The laminar flame velocity is obtained by using cone angle method as follows:

$$S_L = U \cdot \sin(\alpha), \tag{5.3.1}$$

where S_L represents the laminar burning velocity, U is the average velocity of the mixture and α is the cone half-angle as shown in Fig. 5.3.2.

Fig 5.3.2: Experimental laminar burning velocity of methane-air flame with different concentrations and particle size ranges of coal particles.

21

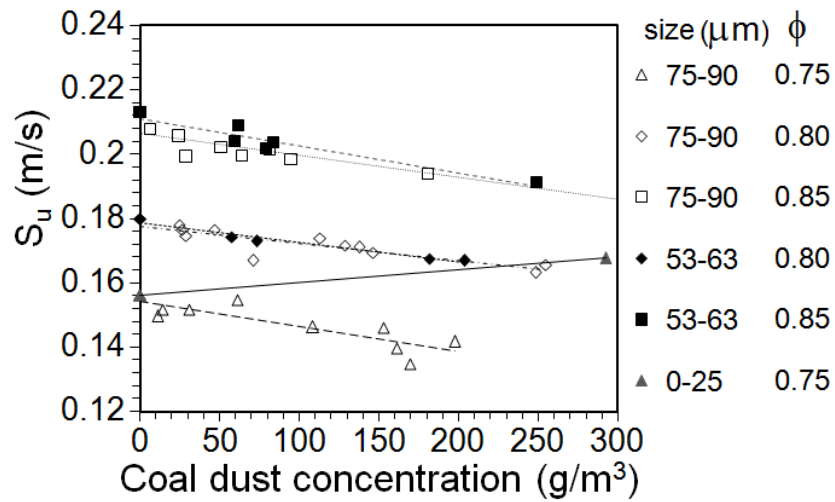It is noted that this method is not the most accurate one to calculate laminar burning velocity; it is used to provide only the trend of variation of laminar burning velocity with equivalence ratio. Since the same method is used to evaluate the laminar burning velocity for all the cases with or without dust injection, the comparison of the trends is expected to be reasonable.

Figure 5.3.2 presents the laminar burning velocity determined from shadowgraph images as a function of the concentration of coal dust. Experiments were conducted for three coal particle size ranges: 75-90 µm, 53-63 µm, and 0-25 µm; and three methane-air equivalence ratios: ϕ = 0.75, 0.8, and 0.85. Due to the strong cohesive forces, the dust entrainment rate is unsteady when smaller particles are employed at low concentrations. Therefore only one data point is obtained using the coal particles in the size range of 0 to 25 µm, at a higher concentration of around 290 g/m^3. In fact, Fig. 5.3.2 shows that the interaction of the coal particles with a laminar premixed methane-air flame reduces S_L when the particle sizes are larger than 25 µm. It is clear that with 0-25 µm coal particles, S_L is promoted as shown by the solid grey triangular symbols, connected by solid line in Fig. 5.3.2. It is demonstrated in Fig. 5.3.2 that the decreasing trend in the slope of S_L for 53-63 µm coal particles is lesser than that with 75-95 µm particles. This indicates that the particle size plays an important role in the problem.

The experiments were also performed with inerts (sand) and heated air (pre-heating). The latter were performed by adding an electric heater to pre-heat the dust-gas-air mixture.

6.0 CONCLUSIONS AND INNOVATION ASSESSMENT

We have developed the *Dust and Gas Explosion Model* (D-GEM) – a computational platform capable of quantifying the mining fire hazards, namely, the probability of spontaneous ignition, the evolution of a flame front, and the likelihood of a deflagration-to-detonation transition. A backbone for the platform is a fully-compressible, finite-volume Navier-Stokes code solving for the hydrodynamics and combustion equations in a homogenously-gaseous, laminar environment. The solver is robust, adapted for parallel computations, and it has been successfully utilized for solving numerous combustion and aero-acoustic problems. The present work initiates the development of the comprehensive D-GEM platform. Specifically, the inert can combustible dust is implemented into the solver by means of thermal-chemical parameters of particle-air flames, tabulated as functions of particle type, size and concentration. In particular, the classical *Seshadri* formulation for the laminar premixed particle-cloud flame speed is employed. It is investigated, systematically, how the noncombustible dust distribution in a mining passage influences the fire evolution, the flame shape and propagation velocity, as well as acceleration rate. The parametric study involves the variety of gradient forms for the dust distribution.

As a separate component of the computational efforts, a computational model is developed to analyze vented explosion scenarios. Such an explosion venting analyzer (EVA) solves the corresponding governing equations in a one-zone approximation, including the external explosion produced once the vented mixture is ignited by the expanding flame, to calculate the attained overpressures in relation to the domain geometry and burning conditions. A parametric study is performed varying the container dimensions and shapes, given by cuboids and cylinders with central and rear ignition locations, and hydrogen in air fuel mixture concentrations. Moreover, different flame velocity expressions are included to account for a variety of effects acting on the flame dynamics. Results show the mitigating effect that the vent has on the enclosure explosion intensity, relating the different conditions to the attained burning regime, essential for the establishment of safety considerations in these partially confined enclosures.

A representative, executable version of the computational platform can be downloaded from http://combustionlab.wpi.edu/EVA.html . Upon request, more details and other versions can be

sent to anyone interested in the solver. The computational research component of the project was closely connected to accompanying analytic and experimental efforts as summarized below.

As an analytic component of the project, the entire scenario of premixed flame front evolution within an accidental fire is prescribed, quantitatively, with the situation of a methane-air explosion in a mining passage as the primary application. Specifically, the key stages of flame evolution are scrutinized. First, a globally-spherical expansion of a centrally-ignited, embryonic flame occurs, with a possibility of self-similar acceleration caused by the hydrodynamic (Darrieus-Landau) instability. This stage provides an order of magnitude increase in the flame speed in realistically large mining passages. Second, a transition from a globally-spherical front to a finger-shaped one happens, when a flame starts approaching the passage walls. While this acceleration is extremely strong, it stops as soon as the flame contacts the passage wall. This mechanism is Reynolds-independent; being equally relevant to micro-channels and realistically large tunnels. Namely, the flame speed increases by one more order of magnitude during this scenario but then stops. Eventually, a flame may accelerate due to wall friction as well as in-built obstacles and wall roughness. While this scenario could be dominant at micro/mesa-scales, it appears negligible in a mining passage because the influence of wall friction decreases, drastically, with the Reynolds number, and wall-attached obstacles are small in mines. Overall, we have identified the key characteristics of all stages such as the timing for each stage as well as the flame shapes, propagation speeds, acceleration rates, run-up distance and flame-generated velocity profiles. The flame propagation speed rises by orders of magnitude. Starting with laminar homogenously-gaseous combustion, the analysis is subsequently extended to dusty-gaseous environments. For this purpose, the dependences of the thermal-chemical flame parameters, such as the planar flame speed, versus the dust properties, such as the dust particles size and concentration, are incorporated into the formulation. Both inert and combustible dust particles are considered.

Phase II of the study comprised of design and construction of an _experimental platform_ to validate and provide input parameters for the numerical model. Turbulent flame propagation is incorporated in a numerical solver using an expression of the forms equations (5.2.5) or (5.2.6). It is important to remember that for any fuel-air mixture, the thermal-chemical flame parameters and hydrodynamic flow parameters have to be known, including additional parameters such as particle concentration, particle size etc. Thus, two experimental directions we were pursued, namely,

(i) Measurement of the laminar burning velocity of dust-gas-air mixtures; and

(ii) Measurement of the turbulent burning velocity of dust-gas-air mixtures

Specifically, the influence of micron-sized (75-90 μm) inert (sand) particles on the laminar and turbulent velocities of methane-air premixed flames of different equivalence ratios (0.9-1.2) and reactant temperatures (297, 350, 400 K) has been undertaken. When an inert particle interacts with the flame zone, it extracts energy from the flame, thereby acting like a heat sink and hence reducing the flame temperature. It is shown that for sand particle size in the range of 75-90 μm, a concentration of 380-520 g/m3 is necessary for extinction of a methane-air flame at ambient temperature. At the same time, an increase in reactant temperature reduces the heat-sink effect necessitating a higher concentration of sand to extinguish the flame.

7.0 REFERENCES

[1] K. Seshadri, A.L. Berlad, V. Tangirala, *The Structure of Premixed, Particle-Cloud Flames*, Combustion and Flame 89 (1992) 333-342.

[2] Y. Xie, V. Raghavan, A.S. Rangwala, *Naturally Entraining Solid Particle Injector*, Powder Technology, 213 (2011) 199-201.

[3] J.T. Botz, C. Loudon, J.B. Barger, J.S. Olafsen, D.W. Steeples, *Effects of Slope and Particle Size on Ant Locomotion: Implications for Choice of Substrate by Antlions*, Journal of the Kansas Entomological Society (2003) 426-435.

[4] D. Bradley, Z. Chen, S. El-Sherif, S.E.-D. Habik, G. John, *Structure of Laminar Premixed Carbon-Methane-Air Flames and Ultrafine Coal Combustion*, Combustion and Flame 96 (1994) 80-96.

[5] G. Andrews, D. Bradley, S.B. Lwakabamba, *Turbulence and Turbulent Flame Propagation – a Critical Appraisal*, Combustion and Flame 24 (1975) 285-304.

[6] B. Lewis, G.V. Elbe, *Stability and Structure of Burner Flames*, Journal of Chemical Physics 11 (1943) 75-97.

[7] S. Goroshin, I. Fomenko, J.H.S. Lee, *Burning Velocities in Fuel-Rich Aluminum Dust Clouds*, Proceding of the Combustion Institute 26 (1996) 1961-1967.

[8] H. Kobayashi, T. Tamura, K. Maruta, T. Niioka, F.A. Williams, *Burning Velocity of Turbulent Premixed Flames in a High-Pressure Environment*, Proceding of the Combustion Institute 26 (1996) 389-396.

[9] V.A. Khramtsov, *Investigation of Pressure Effect on the Parameters of Turbulence and on Turbulent Burning*, Proceedings of the Combustion Institue 7 (1959) 609-620.

[10] S.B. Pope, *Turbulent Premixed Flames*, Annual Reviews on Fluid Mechanics 19 (1987) 237-270.

[11] J. Chomiak, *Basic Considerations in the Turbulent Flame Propagation in Premixed Gases*, Progress in Energy and Combustion Science 5 (1979) 207-221.

[12] V. Akkerman, C.K. Law, V. Bychkov, *Self-Similar Accelerative Propagation of Expanding Wrinkled Flames and Explosion Triggering*, Physical Review E 83 (2011) 026305.

[13] V. Bychkov, V. Akkerman, G. Fru, A. Petchenko, L.-E. Eriksson, *Flame Acceleration at the Early Stages of Burning in Tubes*, Combustion and Flame 150 (2007) 263-276.

Journal Papers

1. S. Ranganathan, M. Lee, V. Akkerman, A. Rangwala, *Extinction of Premixed Flames with Inert Particles*, Journal of Loss Prevention in the Process Industry 35 (2015) 46-51.

2. O. Ugarte, V. Akkerman, A. Rangwala, *A Computational Solver for Gas Explosion Venting*, Process Safety and Environmental Protection, under review.

3. V. Akkerman, S. Demir, S.H.R. Chalagalla, A. Rangwala, V. Bychkov, *Novel Predictive Scenario for Premixed Methane-Air Flame Spreading and Explosion Triggering in a Mining Passage*, to be submitted to Combustion and Flame.

Conference Presentations

1. V. Akkerman, A. Rangwala, V. Bychkov, *Towards Predictive Scenario of Methane and Coal Dust Explosion in a Mining Accident*, 35th International Symposium on Combustion, San Francisco, CA, Aug. 3-8, 2014.

2. V. Akkerman, A. Rangwala, *Dust and Gas Explosion Model for Methane Accidents in Coal Mines*, 31st International Pittsburgh Coal Conference, Pittsburgh, PA, Oct. 6-9, 2014.

3. S. Demir, S.H.R. Chalagalla, V. Akkerman, A. Rangwala, V. Bychkov, *Predictive Scenario for Fires in Gaseous and Dust/Gas Environments: Premixed Flame Evolution*, 40th AIAA Dayton-Cincinnati Aerospace Sciences Symposium, Dayton, OH, USA, Mar. 4, 2015.

4. S.H.R. Chalagalla, S. Demir, V. Akkerman, A. Rangwala, V. Bychkov, *Predictive Scenario for a Methane-Air Fire Spreading in a Mining Passage*, West Virginia Academy of Science (WVAS) Annual Meeting, West Liberty, WV, USA, Apr. 11, 2015. /2nd Paper Award /

5. S. Demir, H. Sezer, B. Demirgok, A. Rangwala, V. Akkerman, *Theory and Modeling of Flame Acceleration Mechanisms for Spatial Variations of Planar Flame Speed*, West Virginia Academy of Science (WVAS) Annual Meeting, West Liberty, WV, Apr. 11, 2015.

6. S. Demir, H. Sezer, B. Demirgok, V. Akkerman, A. Rangwalla, V. Bychkov, *Developing a Computational Platform for Mining Fire Safety*, the West Virginia University's High Performance Computing Meeting, Apr. 16th, 2015. /Best Poster Award/

7. V. Akkerman, S.H.R. Chalagalla, S. Demir, A. Rangwala, V. Bychkov, *Predictive Scenario for Premixed Methane-Air Flame Spreading and Explosion Triggering in a Mining Passage*, 9th US National Combustion Meeting, Cincinnati, OH, May 17-20, 2015.

8. S. Demir, H. Sezer, V. Akkerman, *Effect of Planar Flame Speed Variations on Flame Acceleration Mechanisms*, 9th US National Combustion Meeting, Cincinnati, OH, May 17-20, 2015.

9. S. Demir, H. Sezer, B. Demirgok, A. Rangwala, V. Akkerman, *Towards Modelling of Dusty-Gaseous Fires in Coal Mines*, 9th US National Combustion Meeting, Cincinnati, OH, May 17-20, 2015.

10. O. Ugarte, V. Akkerman, A. Rangwala, *Development of a Computational Explosive Vent Analyzer* (EVA), 9th US National Combustion Meeting, Cincinnati, OH, May 17-20, 2015.

11. S. Demir, V. Akkerman, A. Rangwala, V. Bychkov, *Analysis of Finger Flame Acceleration as a Stage of a Methane-Air-Dust Fire in a Coal Mine*, American Society of Mechanical Engineers (ASME) Power Conference, San Diego, CA, June 28 - July 2, 2015.

Other Documents

- S.H.R. Chalagalla's MS Thesis
- S.H.R. Chalagalla's award document.
- S. Demir's award document.

8.0 APPENDICES

Appendix A: Current Test Standards for Dust Explosion, Necessary Controlling Parameters, and Future Work Related to Bridging the Gap between them

Parameters Involved

	Name of Parameter (symbol, units)	Description	Established Test Methods or Apparatus*
		Thermodynamic Parameters	
1	Heat of combustion (J/g)	Amount of energy released per unit mass undergoing a combustion reaction	Bomb calorimeter
2	Combustion efficiency	Fraction of energy that is utilized in pressure build up	Law of Conservation of Energy
3	Radiant heat fraction	Fraction of total heat released that is transferred via radiation mode	Radiant flux measurements
4	Latent heat of vaporization (J/g)	Amount of heat required to vaporize a unit mass of fuel	Differential Scanning Calorimeter
5	Adiabatic flame temperature (°C)	Maximum possible temperature achieved by the combustion reaction in a constant pressure process	Theoretical Calculations
6	Specific heat of dust (J/g-K)	Amount of energy required per unit mass of dust to increase the temperature of the dust by one unit	Differential Scanning Calorimeter
		Thermo-kinetic Parameters	
7	Laminar burning velocity (m/s)	Velocity at which unburned gases move through a combustion front in the direction normal to the front surface	
8	Propagation speed of smoldering reaction front (m/s)	Rate at which a exothermic oxidation reaction front moves in the direction of non-reactive zone of a dust layer	
9	Rate of reaction in the gas phase (g/s)	Rate at which the reactant gas concentration depletes	
10	Rate of reaction in the solid phase (surface chemical reaction rate) (g/s)	Identifies the smoldering combustion of a dust layer. Smoldering layers can release combustible vapors such as CO, CH4, which can lead to a gas deflagration	
11	Maximum closed volume deflagration pressure (bar)	Maximum pressure reached during a dust deflagration for the optimum concentration of the dust cloud	ASTM E1226
12	Maximum closed volume rate of pressure rise (bar/s)	Rate of pressure rise at maximum pressure reached during a dust deflagration for the optimum concentration of the dust cloud	ASTM E1226
13	Deflagration index, (K_{St}) (bar-m/s)	Rate of pressure rise at maximum pressure during a dust deflagration normalized to unit volume	ASTM E1226
14	Minimum explosion concentration (MEC) (g/m^3)	Minimum concentration of a combustible dust cloud sufficient to increase the pressure by 1 atmosphere (14.7 psi or 1.01bar) due to deflagration. Dust assumed to be well dispersed in air.	ASTM E 1515
15	Minimum ignition energy (MIE) (mJ)	Minimum energy sufficient to ignite most easily ignitable concentration of fuel in air	ASTM E 2019
16	Autoignition temperature of layer (°C)	Lowest set temperature of the surface at which dust layer on it will ignite spontaneously	ASTM E 2021
17	Autoignition temperature of cloud (°C)	Minimum temperature at which a dust cloud will self ignite	ASTM E 1491 06 (Godbert

26

			Greenwald Furnace Test)
18	Limiting oxygen concentration (LOC)	Minimum oxygen concentration at the limit of flammability for the worst case (most flammable) fuel concentration	ASTM E 2079
	Physical Parameters		
19	Thermal conductivity of dust (W/m°C)	Amount of heat transmitted through a unit thickness in a direction normal to a surface of unit area caused due to a unit temperature gradient	
20	Mass of combustible particulate solid (g)	Typically a fugitive dust layer can contain inerts which are not combustible. This property accounts for this variable	
21	Particle shape	Quantitatively, shape factors and coefficients are used as parameters in equations governed by particle shape	Pattern recognition techniques
22	Particle size (m)	Characteristic dimension of irregularly shaped particle representing the diameter of equivalent sphere	Image Analysis with Microscope
23	Particle size distribution	Statistical term that quantifies fluctuations in size and shape of particles of given dust sample	ASTM B761 - 06
24	Bulk density (g/cm^3)	Weight of dust per unit volume	
25	Porosity	Measure of difference in densities of dust bulk and dust particle because of void spaces between particles in the bulk	
26	Degree of compaction of powder	Ratio of volume under specified pressure to volume under ambient pressure for a given mass of dust and configuration of dust pile	
27	Moisture content in dust	Weight percentage of water content in given dust sample	
28	Layer thickness (mm)	Minimum thickness of dust layer of a give particle size needed to cause a deflagration	
29	Surface area/volume ratio of dust (1/m)	Ratio of surface area to volume of given dust particles can be used to relate the arbitrary particle shapes to standard shapes like cube, sphere, cylinder etc.	
30	Suspension	Ease with which particles can be suspended in air	
31	Dispersibility	Degree of dispersion in a dust cloud, depends on cohesiveness of particles, settling velocity, moisture content	ASTM E 1945
32	Agglomeration	A mass conserving, number-reducing process that shifts the particle size distribution towards larger sizes	
33	Terminal settling velocity of dust particle (m/s)	Velocity of a particle when the drag force and buoyancy force balance equal the gravitational pull	
34	Speed of sound in dust cloud (m/s)	Plays an important role in all compressible flow phenomena	
	Chemical Parameters		
35	Chemical composition	Molecular formula of the sample gives important information like Molecular Weight, acidic or basic nature, special affinity for other chemicals	
36	Reactivity with water		
	Electrical Parameters		
37	Volume resistivity	Measure of electrostatic ignition hazard of the dust	IEC 60093
38	Charge relaxation time	Time duration of charge retention in a dust	IEC 61340-2-1:2000
39	Chargeability	Propensity of dust particles to become charged when flowing or air-bourn	IEC 61340-2-1:2000
	External Parameters (facility related)		
40	Size of partial volume	This factor will depend on construction type, volume of	

	explosion that can be handled by the construction	initial cloud that can be formed, number of vents installed, and nature of dust	
41	Type of construction	Based on NFPA 220 standard on types of building construction	
42	Room volume (m^3)	Total volume of room/enclosure where fugitive dust accumulation is possible	
43	Operating temperature (°C)	Certain facilities could operate at a temperature higher than ambient. Thus possibility of autoignition is higher.	
44	Operating pressure (bar)	Certain facilities can operate at pressures other than atmospheric. Studies have shown that thermodynamic and thermo-kinetic properties vary with pressure.	
45	Relative humidity	Major of quantity of water vapor in ambient air	
46	Confinement	Dimensions of the enclosure which is considered to be at constant temperature and pressure and surrounds given test apparatus or control volume under consideration	
47	Turbulence	Flow-instability represented by chaotic state of fluid motion with dissipative structure	
48	Detonability limit	Condition outside which self-sustained propagation of detonation wave cannot be realized	

* Test methods starting with ASTM and IEC are standard test methods (Some standard test methods are not designed for dust per se but can be easily modified to include dust samples)

    i. ASTM B761 – 06: Standard Test Method for Particle Size Distribution of Metal Powders and Related Compounds by X-ray Monitoring of Gravity Sedimentation
    ii. ASTM E 1226 - 05: Standard Test Method for Pressure and Rate of Pressure Rise for Combustible Dust
    iii. ASTM E 1491 – 06: Standard Test Method for Minimum Autoignition Temperature of Dust Clouds
    iv. ASTM 1515 – 07: Standard Test Method for Minimum Explosible Concentration of Combustible Dusts
    v. ASTM E 1945 – 02(2008): Standard test Method for Percent Dispersibility
    vi. ASTM E 2019 – 03(2007): Standard Test Method for Minimum Ignition Energy of a Dust Cloud in Air
    vii. ASTM E 2021 – 06: Standard Test Method for Hot-Surface Ignition Temperature of Dust Layers
    viii. ASTM E 2079 – 07: Standard Test Methods for Limiting Oxygen (oxidant) Concentration in Gases and Vapors
    ix. IEC 60093: Methods of test for volume resistivity and surface resistivity of solid electrical insulating materials
    x. IEC 61340-2-1 (2002-06): Measurement methods – Ability of materials and products to dissipate static electric charge
    xi. IEC 61340-2-2 (2000-067: Measurements methods – Measurement of chargeability

The highlighted rows, No. 7 and No. 47 are fundamental parameters that can be measured for dust-gas-air mixtures using the experimental platform (HFA) developed in the current study. This is a significant breakthrough compared to existing test apparatuses such as the 20 lt or 1 m3 explosion sphere which is currently used to determine an empirical deflagration index (K_{ST}) which is difficult to incorporate in standards compared to the more fundamental thermokinetic property such as laminar burning velocity.

To give an example of the applicability of this output, an example of the historical development of the National Fire Protection Association Code NFPA 68: Standard on Explosion Protection by Deflagration Venting will be employed. Note that this standard is used for both deflagration venting of gasses (Chapter 7) as well as dusts (Chapter 8). An important criteria for deflagration vent design is the area of the vent necessary such that given a deflagration (gas or dust or hybrid) what is the minimum area necessary to vent the explosion safely without damage to the structure. Obviously, the larger the vent area the more expensive is the deflagration vent. In the 1998 version of the NFPA 68 code, the equation used to estimate the vent area for gas deflagrations is given by:

$$A_v = [(0.0127 \log_{10} K_G - 0.0567) P_{red}^{-0.582} + 0.175 P_{red}^{-0.572} (P_{stat} - 0.1)] V^{2/3}, \quad (2)$$

where, P_{red} is the maximum pressure developed during the venting, P_{stat} is the static activation pressure of the vent and most importantly K_G is the deflagration index or explosion constant of the gas-air mixture obtained using the 20 lt explosion sphere. Note that K_G is defined similar to Eq. 1, with the only difference that in this case we are dealing with a gas and not a dust. The disadvantage of using the deflagration index were soon realized and gradual improvements were made to the overall design equation for vent area such that fundamental parameter of laminar and turbulent burning velocities were incorporated after several studies. A perusal of NFPA 68, 1998, 2002, 2007 and 2013 editions will demonstrate this effort clearly. The equation that is used in the current (NFPA 68, 2013) version of the code is of the form $A_v = f(S_u, P_{red}, P_{stat}, \lambda)$, where S_u represents the laminar burning velocity of the gas-air mixture (maximum value) and λ denotes the ratio of gas air turbulent burning velocity to laminar burning velocity. The reason this change was possible, is because of the ease with which laminar and turbulent burning velocity of gas-air mixtures can be measured. Several techniques are available and correspondingly experimental platforms related to this measurement are available due to the extensive work performed in premixed gas flame combustion literature.

The same cannot be said for Chapter 8 of NFPA 68 which provides equations for designing vent area for dust deflagrations. In the current version of NFPA 68 (2013) the equations still rely on the deflagration index (K_{st})! This problem exists because there is no experimental apparatus currently in place that can measure the burning velocity (laminar and turbulent) of dust-air flames. Work by Goroshin et al.[1], and Dobashi and Senda[2] has progressed to some extent in developing experiments to measure laminar burning velocities. However these studies are limited in the range of dust particles, types and concentrations that can be used. The DFA proposed in this study is applicable to a wide range of dusts, and povides both laminar and turbulent burning velocity data. Ultimately this data will be converted into an engineering tool which can be applied to codes such as NFPA 68.

Moving forward:

Currently NFPA 654 (Standard for Prevention of Fire and Dust Explosion from the Manufacturing, Processing and handling of Combustible Solid Particles) and 664 (Standard for the Prevention of Fires and Explosions in Wood Processing and Woodworking Facilities) list the following parameters that are used to identify a dust explosion hazard:
   1. Minimum explosion concentration, MEC (3.3.16, NFPA 654 and A.3.3.9.2, NFPA 664)
   2. Minimum ignition energy (MIE) (A.3.3.9.2, NFPA 664)
   3. Particle size distribution (A.3.3.9.2, NFPA 664)
   4. Moisture content (A.3.3.9.2, NFPA 664)
   5. Maximum explosion pressure at optimum concentration (A.3.3.9.2, NFPA 664)
   6. Maximum rate of pressure rise at optimum concentration (A.3.3.9.2, NFPA 664)
   7. Deflagration index or K_{St} (A.3.3.9.2, NFPA 664)

[1] S. Goroshin, I. Fomenko, J.H.S. Lee, Burning Velocities in Fuel-Rich Aluminum Dust Clouds, in: Proc. Combust. Inst., The Combustion Institute, 1996, pp. 1961-1967.
[2] R. Dobashi, K. Senda, Detailed analysis of flame propagation during dust explosions by UV band observations, Journal of Loss Prevention in the Process Industries, 19 (2006) 149-153.

8. Depth of dust accumulation (Table A.6.6.2, NFPA 654)
9. Layer ignition temperature (A.3.3.9.2, NFPA 664)
10. Dust cloud ignition temperature (A.3.3.9.2, NFPA 654)
11. Limiting oxidant concentration to prevent ignition (A.3.3.9.2, NFPA 654)
12. Electrical resistivity (A.3.3.9.2, NFPA 654)
13. Charge relaxation time (A.3.3.9.2, NFPA 654)
14. Chargeability (A.3.3.9.2, NFPA 654)
15. Minimum dust accumulation area (A.6.4.2.2 (2), NFPA 654)
16. Lowest temperature at which pyrolysis has been reported (5.2.4.1, NFPA 654)
17. Minimum dust accumulation thickness(0.8 mm -6.2.3.1, NFPA 654 and 3.2 mm - 6.4.2.2, NFPA 664)

As a first step, it is important to identify parameters out of this list of 17 that are most important and relevant to the problem at hand. It should be noted that the minimum dust layer thickness which is the main basis for identifying a dust hazard in NFPA 654, characterizes the quantity of fugitive dust that can reasonably be suspended by a single credible upset[3] vs. the room volume it can be suspended in. This quantity however does not characterize the properties of dust and also suffers from identifying a minimum threshold. The threshold in this approach would be the quantity where the over-pressure resulting from the explosion does not result in damage beyond the initiating area. Thus additional parameters such as size of a partial volume explosion that can be handled by the construction need to be included. Such additional parameters are included in Appendix A where a first attempt at documenting all the parameters involved in the problem (48 parameters total) are listed.

Overall, the parameters in Appendix A are grouped into thermodynamic, thermokinetic, physical, chemical, and electrical properties of the dust. In addition, facility related parameters such as type of construction, confinement level, operating temperature, humidity in air etc: are also accounted. Thermodynamic properties are heat of combustion, adiabatic flame temperature, specific heat, thermal conductivity, and latent heat of vaporization. Thermokinetic properties are based on both the thermodynamic and chemical kinetic effects. For example, the laminar burning velocity[4] depends on both thermodynamic (heat of combustion) as well as chemical kinetic (rate of gas phase reaction) processes. Physical properties include mass of particles, particle size, ease of suspension etc. Chemical properties include parameters used to quantify chemical composition of the dust. Dust deflagrations are also sensitive to electrical properties of the dust which determine the ease of charge dissipation and charge storage to analyze static electric ignition. Facility related parameters include construction type, confinement levels etc. It could be argued that all 48 parameters listed in Appendix A are important and need to be known to quantify a hazard associated with a dust. However, a more rational engineering approach would be to make an optimal choice of these parameters based on:

1. How important is the effect of these parameters on the explosion outcome
2. How variable are these parameters among most common materials susceptible to dust explosions
3. How much resolution is really needed for adequate design in practice

---

[3] Upsets are, for example, a compressed air line lets loose and the turbulence forms a cloud of fugitive dust that had accumulated on equipment tops and bar joists.

[4] Laminar burning velocity also called flame velocity, normal combustion velocity, or laminar flame speed is defined as the velocity of at which the unburned gases move through the combustion wave in the direction normal to the wave surface

Some of the parameters listed in Appendix A will thus drop out and a list of main controlling factors of a dust hazard will be obtained. A series of methodologies to assess the resulting parameters can then analyzed proposing an optimal set of tests that will lead to the quantification of these parameters. The resulting parameters could then be incorporated into a dust hazard analysis guideline to establish impact, but impact assessment needs to be related to existing impact assessment methodologies:

4. How adequate are the testing methodologies in isolating and quantifying these parameters, propose viable improvements
5. How good are the impact testing methodologies currently used when assessing the outcome
6. Can the testing methodologies be improved based on the recent advances in measurement techniques and diagnostic tools

An example test scheme is shown below. The test scheme is based on characterizing the dust as well as the facility is shown in Figure 1a and 1b. A dust hazard assessment guide similar to the Fire Safety Analysis Manual for LP-Gas Storage Facilities[5] is needed for coal mines. The manual will be intended for use by facility owners, operators, consultants and authorities having jurisdiction and will address the process by which a dust explosion hazard assessment can be conducted by a facility handling combustible dusts.

---

[5] Developed by National Fire Protection Association and National Propane Gas Association, by Raj and Lemoff (2006)
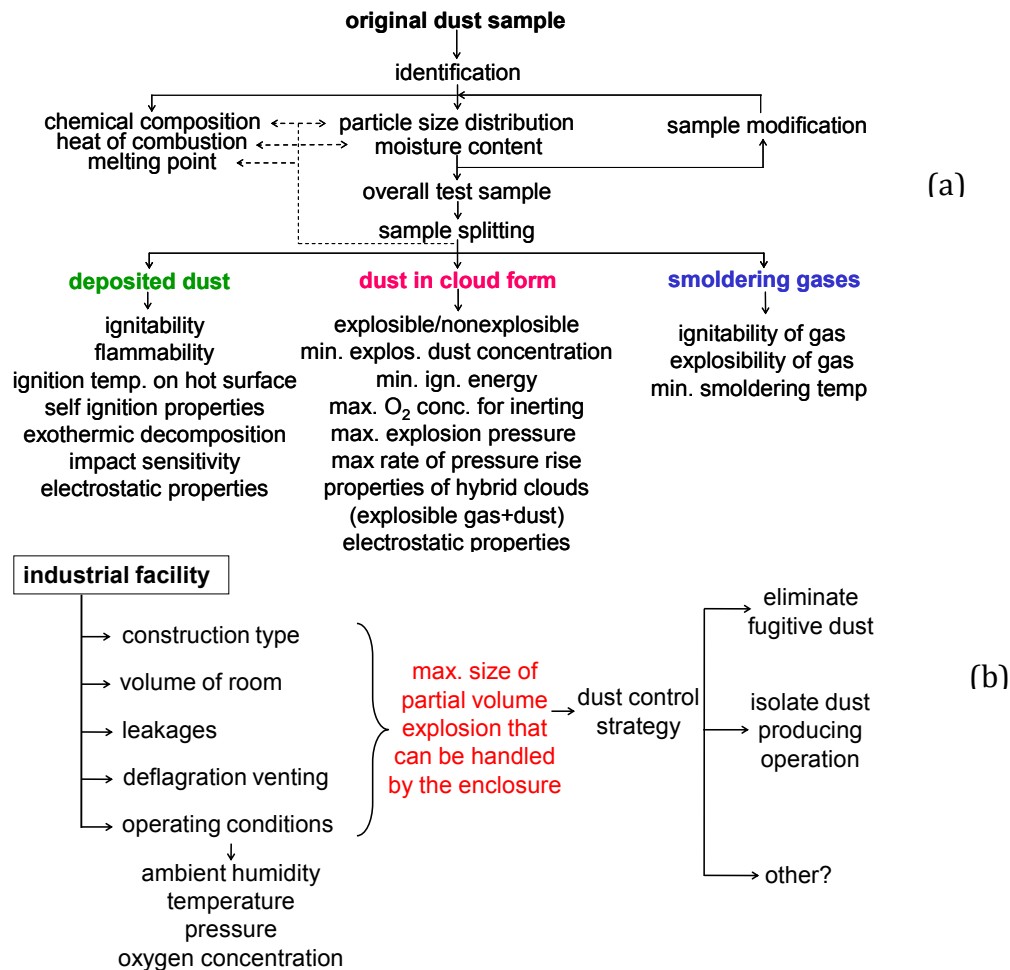
Figure 1: (a) Flowchart of possible tests for assessing the ignitability and explosibility of dusts and (b) parameters associated with the facility.

Once a manual on assessing dust hazard in a facility is prepared, guidance on future research, experimentation (small, large and intermediate scale), and modeling (numerical and analytical) results can be used.

9.0 ACKNOWLEDGEMENT/DISCLAIMER